Tunable lumped element notch filter for UHF communications systems

by

Peter-Luke Benson

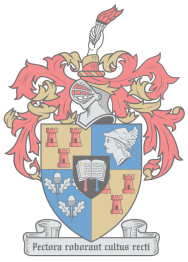

Thesis presented in full fulfilment of the requirements for the degree of Master of Engineering (Electronic) in the Faculty of Engineering at Stellenbosch University

Supervisor: Prof. P. Meyer

March 2018

Declaration

By submitting this thesis electronically, I declare that the entirety of the work contained therein is my own, original work, that I am the sole author thereof (save to the extent explicitly otherwise stated), that reproduction and publication thereof by Stellenbosch University will not infringe any third party rights and that I have not previously in its entirety or in part submitted it for obtaining any qualification.

Date: March 2018 .....

Abstract

Tunable lumped element notch filter for UHF communications systems

P. Benson

Department of Electrical and Electronic Engineering,
University of Stellenbosch,
Private Bag X1, Matieland 7602, South Africa.

Thesis: MEng (Electronic)

December 2017

This thesis presents a study on a tunable lumped element notch filter. The purpose of the filter is to be placed at the frontend of a receiver to suppress unwanted communications channels in the UHF PMR frequency band of 400-490MHz such to minimise desensitisation of the receiver. Different filter response types are studied and a comparison is drawn up from which the Chebyshev (0.5dB ripple) response is found to be the best to implement. The stopband performance of the filter is evaluated for resonators with different unloaded Q-factors. The final design is implemented on a low loss PCB with surface mount lumped elements and semiconductors. Tuning of the notch is implemented using varactor diodes to change the resonant frequency of the resonators in the filter. The nonlinear behaviour of the filter due to the varactor diodes is investigated. From the final results, a tuning range of 400-460MHz is obtainable with a notch attenuation of 10dB at the lowest tuned frequency and 20dB at the highest tuned frequency. The third-order intercept point is determined as 26dBm and the spurious free dynamic range (SFDR) is determined as 77dB.

Uittreksel

Verstelbare diskreet komponent nouband bandstopfilter vir UHF kommunikasie stelsels

P. Benson

Departement Elektries en Elektroniese Ingenieurswese,
Universiteit van Stellenbosch,
Privaatsak X1, Matieland 7602, Suid Afrika.

Tesis: MIng (Elektronies)

Desember 2017

Hierdie tesis behels die studie van 'n verstelbare diskreet komponent nouband bandstopfilter. Die doel van die filter is om voor 'n ontvanger geplaas te word en ongewenste komunikasie kanale in die UHF PMR band te onderdruk. Verskillende filter gedragte word ondersoek en dit is gevind dat die Chebyshev (0.5dB rippel) die beste is om te implementeer. Die stopband verswakking van die filter is geövalueer vir resoneerders met verskillende ongelaaide Q-faktore. Die finale ontwerp is geimplementeer op 'n laeverlies PCB met oppervlak komponente. Die verstelbaarheid van die filter is geimplementeer met varaktor diodes wat die resonante frekwensie van die resoneerders verander. Die nie-lineêre gedrag van die filter as gevolg van die varaktor diodes is ondersoek. Vanaf die finale resultate, kan die filter tussen 400-460MHz verstel word met 'n nul verswakking van 10dB by 400MHz en 20dB by 460MHz. Die derde-orde afsnitpunt is berken as 26dBm met 'n vals vrye dinamiese reeks van 77dB.

Acknowledgements

I would like to thank Prof Meyer for his mentorship and patience throughout this project.

I would also like to thank Dr Cornell van Niekerk for his mentorship and advice and to GEW for the sponsorship of this project.

Lastly, I would like to thank my family and friends who have supported me throughout this project.

Contents

List of Figures

List of Tables

List of Abbreviations

ADS	Keysight Technologies Advanced Design System
AGC	Automatic gain control
ESR	Equivalent series resistance
IM	Intermodulation
LDR	Linear dynamic range
LNA	Low noise amplifier
LPF	Lowpass filter
MDS	Minimum detectable signal
PMR	Personal Mobile Radio
RF	Radio frequency
SFDR	Spurious free dynamic range
SRF	Self resonant frequency
UHF	Ultra high frequency
VHF	Very high frequency

Chapter 1

Introduction

Notch filters are bandstop filters with the primary purpose of filtering out unwanted signals that lie in a narrow frequency band. A common application of such filters at very low frequencies is to filter out mains power signals (50/60Hz) from audio signals. For radio frequency (RF) applications, these filters can be used to filter out unwanted communications channels for receivers or to suppress out-of-band interference signals generated by transmitters. This thesis presents the design of a tunable lumped element RF notch filter to be operated in the UHF personal mobile radio (PMR) frequency band. The project background, objectives and thesis layout are discussed in this chapter.

1.1 Project background

Communication systems play a vital role in military operations to facilitate the transfer of information. The use of electronic systems to undermine an adversary's communication systems and/or to defend the integrity of one's own communication systems is termed *electronic warfare* (EW) [1]. There are three forms of EW: *electronic attack* (EA), *electronic protection* (EP) and *electronic support* (ES) [2].

A particular application of EA is ground based signal jamming illustrated in figure 1.1. A basic diagram of a jammer system with a monostatic antenna configuration is shown in figure 1.2. The jammer scans the EM spectrum for signals coming from potential targets using its search receiver. Detected signals are sampled by the signal processing unit where they are interpreted and a decision is made. Once a decision is made, the signal processing unit sends a control signal to the exciter which generates the desired jamming signal. The jamming signal is amplified by the power amplifier and then radiated out from the antenna [3, 4].

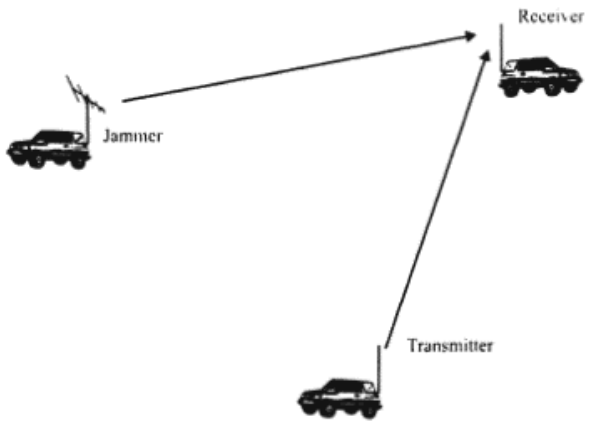

Figure 1.1: Illustration of ground based signal jamming

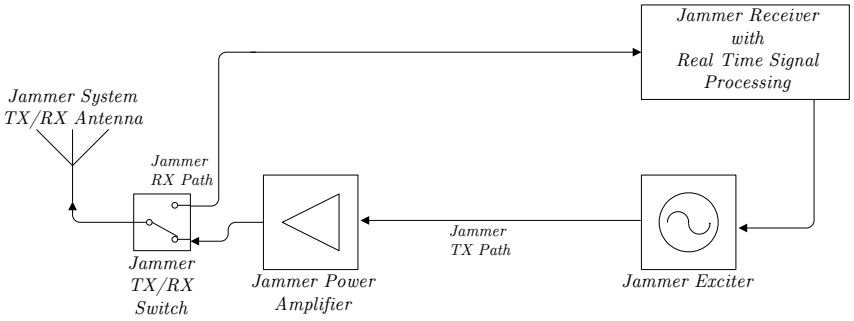

Figure 1.2: Basic diagram of a jammer system

A jammer system can be used to target the receivers of an adversary's communications systems by denying the use of certain frequency bands in the EM spectrum. This is achieved by radiating high levels of noise power from the jammer system to reduce the signal-to-noise ratio (SNR) at the target receiver preventing it from extracting the information it requires [1, 2]. There are two problems asociated with this form of EA: firstly, fratricide occurs when the receivers of friendly communication systems are influenced by the jammer and secondly, the receiver of the jammer system becomes desensitised when it detects strong signals from nearby friendly communications systems [5,6]. Desensitisation essentially reduces the receiver's ability to detect weak signals from potential targets that are far away. Two approaches are used to mitigate these problems. In [7], an application of EP has resolved the problem of fratricide occurring with the design of an active noise cancellation system that subtracts the jammer noise from incoming signals at the front end of the friendly communications receivers shown in figure 1.3. The remaining problem pertaining to the desensitisation of the jammer receiver is addressed in this thesis. A basic overview of a typical receiver system shall now be discussed in order to give insight into how the performance of a receiver is characterised.

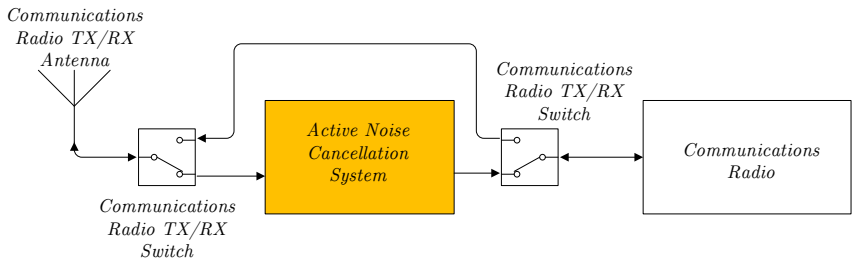

Figure 1.3: Basic diagram of a communications system with active noise cancellation

A basic diagram of a dual-conversion superheterodyne receiver is shown in figure 1.4. The incoming signals are amplified and filtered in stages to prepare them for either demodulation or digital sampling. Automatic gain control (AGC) measures are incorporated to compensate for variations in input signal power to ensure that the amplifiers operate in their linear regions [8]. Saturation of the amplifiers would cause undesireable signal distortion at the output of the receiver. The workings of the receiver can be simplified and modelled as a single stage amplifier with AGC having power transfer characteristics shown in figure 1.5 [9]. The range of the signal power (input or output) that falls within the linear region of operatation is termed the *linear dynamic range* (LDR) [10]. The LDR with respect to signals at the input of the receiver is

$$\text{LDR (dB)} = \text{Pin}_{\text{max}}(\text{dBm}) - \text{Pin}_{\text{min}}(\text{dBm}), \tag{1.1.1}$$

where Pin_{max} is the maximum allowed input signal power and Pin_{min} is the minimum detectable signal (MDS) power [8, 11]. The LDR of a receiver is typically fixed and does not change with variations of the system gain. The boundaries of the input power described in equation 1.1.1, however, do change with variations of the system gain [9]. If a strong signal was suddenly detected by the receiver, the system gain would be decreased to compensate for this resulting in an increase in both the Pin_{max} and Pin_{min} boundaries. The sensitivity of the receiver is based on the power level of Pin_{min} and so an increase in this boundary would result in desensitisation of the receiver [1].

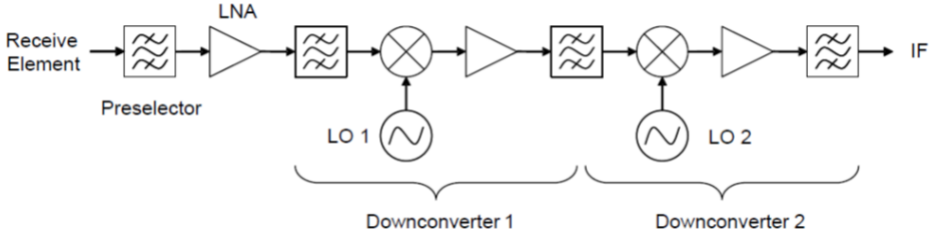

Figure 1.4: Basic diagram of a dual-conversion superheterodyne receiver

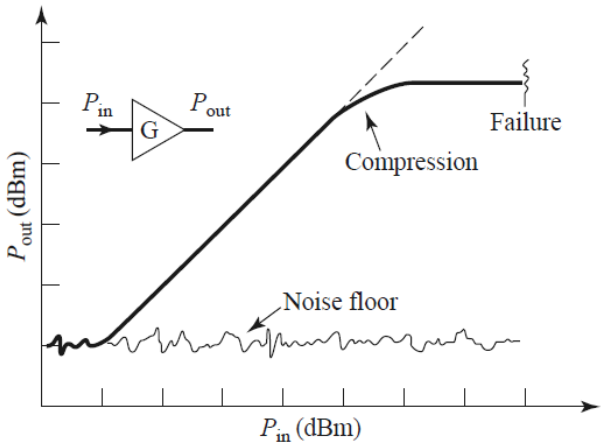

Figure 1.5: Graphical representation of power transfer characteristics for a typical amplifier

The receiver of the jammer has a fixed LDR of 70dB. The typical noise floor at the input of the receiver is -100dBm [4]. By basing Pin_{min} on this value and using equation 1.1.1, the best receiver sensitivity is possible when Pin_{max} is no greater than -30dBm. As stated earlier, the use of friendly communications systems in the vicinity of the jammer system is the primary contributer towards the receiver becoming desensitised. To understand the extent of the desensitisation, three widely used military communication systems are investigated [12–14]. The specifications of these communication systems are shown in table 1.1.

Table 1.1: Specifications of widely used military communication systems

System	Frequency range [MHz]	Max Tx power [dBm]
VX-160EU/-180EU	400-490 (UHF PMR)	37
VX-160EV/-180EV	134-174 (VHF PMR)	37
Leopard I	1.6-512 (wideband)	45

The antenna coupling, C_{ant}, between the jammer and nearby communications systems is in the order of -20dB [4]. From the specifications in table 1.1, the Leopard I has the highest transmission power, Tx_{max}. For a worst-case scenario, the upper input power boundary of the jammer receiver can be determined as

$$\text{Pin}_{\text{max}} = \text{Tx}_{\text{max}} + \text{C}_{\text{ant}} = 25\text{dBm}, \tag{1.1.2}$$

which means that Pin_{min} is -45dBm for a LDR of 70dB. This is a 55dB decrease in sensitivity from the best-case scenario.

1.2 Project objectives

The main objective of this project is to reduce the desensitisation of the jammer receiver. This can be achieved by placing a notch filter at the front end of the receiver in order to suppress incoming signal power in communications channels that are being utilised by friendly communications systems shown in figure 1.6. The ideal null rejection required to reduce $\mathrm{Pin}_{\max}$ at the receiver front end based on a worst-case scenario is

$$\alpha = \mathrm{Tx}_{\max} + \mathrm{C}_{\mathrm{ant}} - \mathrm{LDR} - \mathrm{Pin}_{\min} = 55\mathrm{dB}. \tag{1.2.1}$$

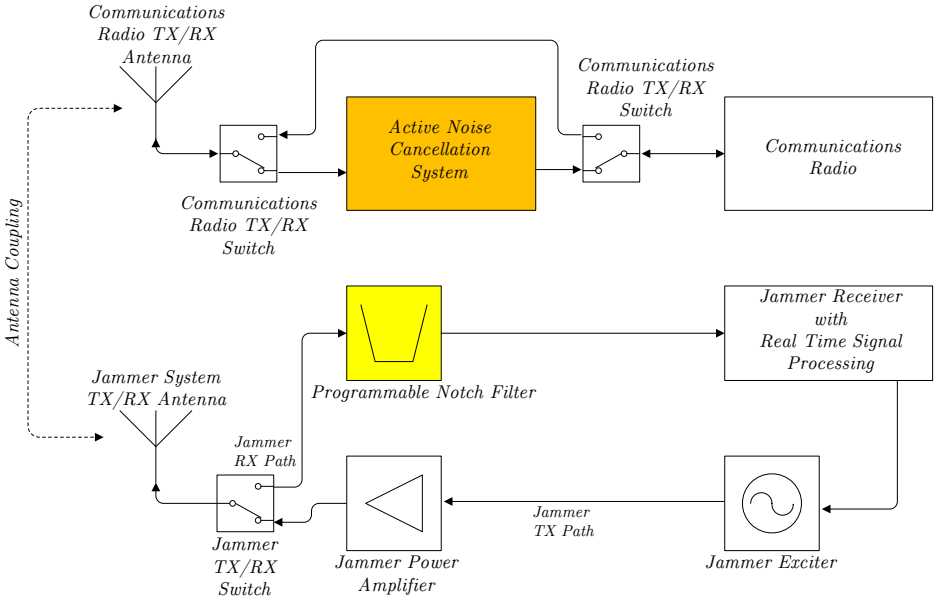

Figure 1.6: Optimal EW system diagram with active noise cancellation for communications system and notch filter module for jammer system

The jammer operates over a wide band of 20-500MHz. A single tunable notch filter would be difficult to implement over this range as it would require a frequency tuning ratio of 1:25. Instead, a better approach is to implement a filter bank consisting of different tunable notch filters where each has a tuning range designated to a specific frequency band. The three most commonly used frequency bands for military communication systems are 30-88MHz (VHF), 134-174MHz (VHF PMR) and 400-490MHz (UHF PMR). This thesis will focus exclusively on the design, implementation and measurement of a tunable notch filter for the 400-490MHz (UHF PMR) band. In [15], a second-order tunable lumped element notch filter with a tuning range of 470-730MHz and 16dB null rejection has been documented. From this research, it is noted that the null rejection is dependant on the quality (Q) factors of the resonators that are used in the filter. The frequency range is too low to use high-Q distributed elements as this would result in a physically large network.

Instead, lumped elements are the preferred components to use due to their more compact size even though their Q-factors are significantly lower than those of distributed elements. Rather than having rigid specifications placed on the design, the goal is to determine the type of performance that can be achieved with components currently available. The ideal null rejection is too high of a requirement to achieve with a single low-order filter, but could be achieved with multiple filters in cascade.

1.3 Thesis structure

This thesis is structured over six chapters. Chapter 2 presents background filter theory and discusses the synthesis of a lossless fixed frequency notch filter. The insertion loss method is used to characterise the transfer characteristics of the filter from a purely mathematical perspective. A set of design equations is derived to realise a circuit model that can implement the desired transfer characteristics.

Chapter 3 discusses the practical implementation of the circuit model derived in chapter 2. The circuit model is revised to incorporate tuning. A section is presented on the behaviour of non-ideal components in order to assist with making informed decisions regarding component selection. Modelling techniques for non-ideal components are discussed and implemented in simulations to accurately predict the behaviour of the filter.

Chapter 4 presents theory on the non-linear behaviour of systems. The impact that non-linear behaviour has on the filter performance is investigated.

Chapter 5 presents and discusses the practical measurements that were taken from the actual filter that was built. Diagnostics are performed and modifications are made to enhance the performance of the filter.

Chapter 6 concludes the thesis by providing a final verdict on the filter. Recommendations are presented for future work and system integration.

Chapter 2

Filter Synthesis

This chapter will discuss the synthesis of a lossless fixed frequency notch filter. A black box approach is initially pursued to describe the filter purely in terms of its transfer characteristics using the insertion loss method for filter synthesis. Different types of transfer characteristics are investigated and compared to determine a simple and working solution that can meet the core specifications of the design. A circuit model is derived to implement the desired filter response using lumped element resonators. The chapter concludes by evaluating the impact that lossy resonators can have on the overall performance of the filter. The practical implementation of the filter design using non-ideal lumped components and semiconductors will be discussed in the next chapter.

2.1 Two-port S-parameters

A filter can be treated as a passive two-port network. For RF and microwave systems, scattering (S) parameters are used to characterise two-port networks instead of impedance (Z) or admittance (Y) parameters. Impedance and admittance parameters are based on total voltage and current measurements at each port of a network. For the mesurement at a given port, this requires that all other ports be terminated with either open or short circuits. The shortcomings of this is that open and short circuit terminations cannot be realised accurately at high frequencies and may cause undesirable behaviour particularly with active networks [16, 17]. S-parameters are based on the ratios of forward and backward travelling voltage waves on transmission lines connected to the ports of a network [9, 18]. For the measurement of S-parameters, resistive terminations corresponding to the characteristic impedance of the measuring system are used, which for the general case, is 50Ω [17]. A block representation of such a two-port network is presented in figure 2.1.

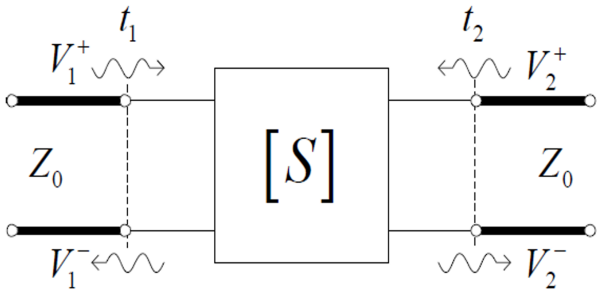

Figure 2.1: Block representation of a two-port network

If Z_0 is the same at both ports, then the travelling waves and S-parameters can be expressed in a matrix equation as follows:

$$\begin{bmatrix} V_1^- \\ V_2^- \end{bmatrix} = \begin{bmatrix} S_{11} & S_{12} \\ S_{21} & S_{22} \end{bmatrix} \begin{bmatrix} V_1^+ \\ V_2^+ \end{bmatrix}, \tag{2.1.1}$$

where V_{n}^+ is the forward travelling voltage wave towards the specified port and V_{n}^- is the backward travelling voltage wave away from the specified port.

The S-parameters for equation 2.1.1 can be determined by terminating each port with a matched load. For the case where port 2 is terminated with a matched load, $V_2^+ = 0$ due to no reflections from the load. The following S-parameters can be determined:

$$S_{11} = \left.\frac{V_1^-}{V_1^+}\right|_{V_2^+=0} = \Gamma_{11} \tag{2.1.2}$$

and

$$S_{21} = \left.\frac{V_2^-}{V_1^+}\right|_{V_2^+=0} = T_{21}, \tag{2.1.3}$$

where S_{11} is the reflection coefficient of port 1 and S_{21} is the transmission coefficient from port 1 to port 2. It is important to reiterate that equations 2.1.2 and 2.1.3 are only valid when port 2 is matched. In a similar manner, S_{22} and S_{12} can be determined by terminating port 1 with a matched load [9]. A network is symmetrical when $S_{11} = S_{22}$ and reciprocal when $S_{21} = S_{12}$ [16].

When port 2 is matched, the total time average power at port 1 is comprised of the incident power, P_{inc}, and reflected power, P_{ref}, whilst the total time average power at port 2 is the transmitted power, P_{tran} [18].

$$P_{\text{inc}} = \frac{|V_1^+|^2}{2Z_0} \tag{2.1.4}$$

$$P_{\text{ref}} = \frac{|V_1^-|^2}{2Z_0} \tag{2.1.5}$$

$$P_{\text{tran}} = \frac{|V_2^-|^2}{2Z_0} \tag{2.1.6}$$

For a lossless passive two-port network, the conservation of power must hold true which implies that the power that enters the ports of the system must equal the power that leaves the ports of the system [18].

$$P_{\text{inc}} = P_{\text{ref}} + P_{\text{tran}} \tag{2.1.7}$$

$$\frac{|V_1^+|^2}{2Z_0} = \frac{|V_1^-|^2}{2Z_0} + \frac{|V_2^-|^2}{2Z_0}$$

$$1 = \frac{|V_1^-|^2}{|V_1^+|^2} + \frac{|V_2^-|^2}{|V_1^+|^2}$$

$$1 = |S_{11}|^2 + |S_{21}|^2 \tag{2.1.8}$$

Equation 2.1.8 shows the relationship between the S-parameters and the per unit relative time average power at the ports. If unit power flows into port 1, a fraction $|S_{11}|^2$ is reflected and a fraction $|S_{21}|^2$ is transmitted [16].

2.2 Characterisation of filter by insertion loss

A filter can be characterised by its magnitude and phase or group delay responses [19]. This section will focus on characterising a filter by its insertion loss (IL) which describes the filter's magnitude response in terms of the relative power loss in its transmission path. A lossless filter with an input impedance, $Z_{\text{in}}(\omega)$, and reflection coefficient, $\Gamma(\omega)$, at port 1 is shown in figure 2.2.

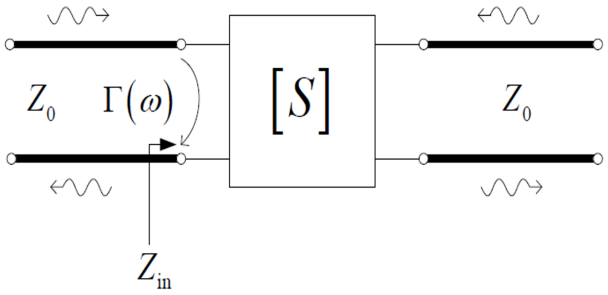

Figure 2.2: Two-port representation of a filter with port 1 as the input

The reflection coefficient is defined as

$$\Gamma = \frac{Z_{\text{in}}(\omega) - Z_0}{Z_{\text{in}}(\omega) + Z_0}. \tag{2.2.1}$$

The power loss ratio, P_{LR}, is defined as the ratio between the incident power at port 1, P_{inc}, and the power transferred to the network, P_{load} [10, 18].

$$\begin{aligned} P_{\text{LR}} &= \frac{P_{\text{inc}}}{P_{\text{load}}} \qquad (2.2.2) \\ &= \frac{P_{\text{inc}}}{P_{\text{inc}}(1 - |\Gamma(\omega)|^2)} \\ &= \frac{1}{1 - |\Gamma(\omega)|^2} \\ &= \frac{1}{|T(\omega)|^2} \qquad (2.2.3) \end{aligned}$$

The insertion loss in dB is defined as

$$\begin{aligned} \text{IL} &= 10\log(P_{\text{LR}}) \\ &= -20\log|T(\omega)|. \qquad (2.2.4) \end{aligned}$$

If the system is matched at both the source and load ports then equation 2.2.4 can be expressed in terms of the filter's $S_{21}(\omega)$ parameter as

$$\text{IL} = -20\log|S_{21}(\omega)|. \tag{2.2.5}$$

The advantages of characterising a filter by its insertion loss allows for a purely mathematical description of the filter's magnitude response for power transfer without the need of a circuit model.

2.3 Overview of ideal filter response types

The most common procedure to realise a desired filter response with specific passband and stopband attributes is to start with a reference lowpass response called the prototype [20]. The prototype represents a normalised filter with a unitary cut-off frequency ($\Omega_c = 1$) and input impedance ($R_S = 1$). The ideal "brick wall" prototype response has unitary transmission (zero insertion loss) in its passband and zero transmission (infinite insertion loss) in its stopband illustrated in figure 2.3 [16]. The transmission coefficient is a piecewise function described by equation 2.3.1.

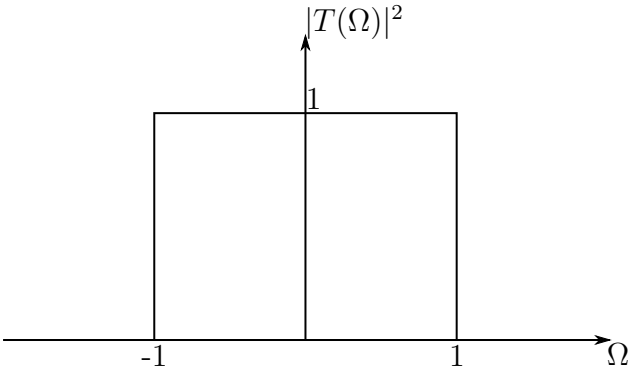

Figure 2.3: Ideal lowpass prototype response

$$|T(\Omega)|^2 = \begin{cases} 1 & |\Omega| < 1 \\ 0 & |\Omega| > 1 \end{cases} \tag{2.3.1}$$

Other filter response types can be obtained by applying frequency transformations to the prototype [20]. The frequency transformations map the values of the desired filter response to the values of the prototype.

2.3.1 Ideal lowpass filter response

An ideal lowpass filter with a desired cut-off frequency, ω_c, can be obtained by applying the frequency transformation specified by equation 2.3.2 [10].

$$\Omega \leftarrow \frac{\omega}{\omega_c} \tag{2.3.2}$$

The resulting lowpass response is illustrated in figure 2.4 with the function mappings illustrated in table 2.1.

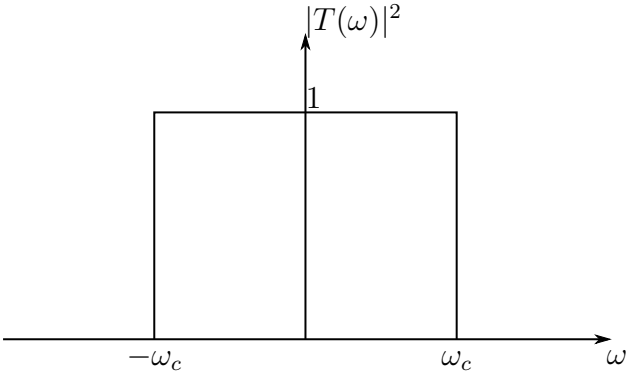

Figure 2.4: Ideal lowpass filter response

Table 2.1: Function mappings for lowpass frequency transform

$\boldsymbol{\Omega}$	$-\infty$	-1	0	1	∞
$\boldsymbol{\omega}$	$-\infty$	$-\omega_c$	0	ω_c	∞

2.3.2 Ideal highpass filter response

An ideal highpass filter with a desired cut-off frequency, ω_c, can be obtained by applying the frequency transformation specified by equation 2.3.3 which is the inverse of a lowpass transformation [10].

$$\Omega \leftarrow \frac{-\omega_c}{\omega} \tag{2.3.3}$$

The resulting highpass response is illustrated in figure 2.5 with the function mappings illustrated in table 2.2.

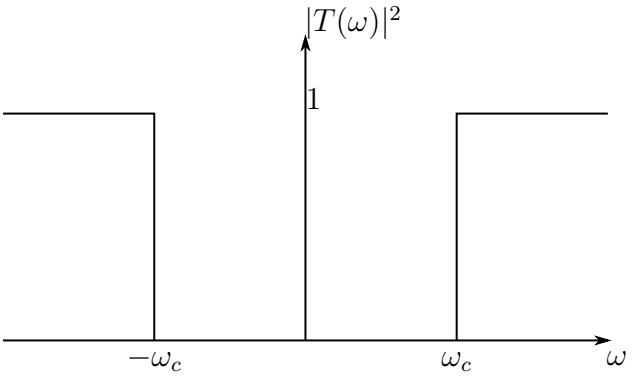

Figure 2.5: Ideal highpass filter response

Table 2.2: Function mappings for highpass frequency transform

$\boldsymbol{\Omega}$	$-\infty$	-1	0	1	∞
$\boldsymbol{\omega}$	0	ω_c	$\pm\infty$	$-\omega_c$	0

2.3.3 Ideal bandpass filter response

An ideal bandpass filter with a desired passband bound by lower corner frequency, ω_1, and upper corner frequency, ω_2, with centre frequency, $\omega_0 = \sqrt{\omega_2\omega_1}$, can be obtained by applying the frequency transformation specified by equation 2.3.4 which has multiple mappings to the same prototype value [10, 20].

$$\Omega \leftarrow \frac{1}{\Delta}\left(\frac{\omega}{\omega_0} - \frac{\omega_0}{\omega}\right) \tag{2.3.4}$$

The fractional bandwidth, Δ, is defined as

$$\Delta = \frac{\omega_2 - \omega_1}{\omega_0}. \tag{2.3.5}$$

The resulting bandpass response is illustrated in figure 2.6 with the function mappings illustrated in table 2.3. The same bandpass response could be achieved by a separate highpass filter with $\omega_c = \omega_1$ cascaded with a lowpass filter with $\omega_c = \omega_2$.

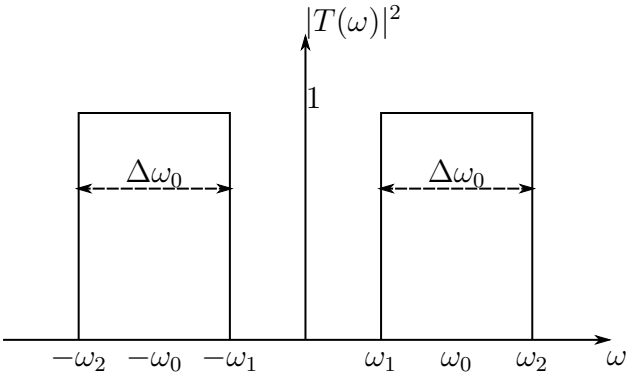

Figure 2.6: Ideal bandpass filter response

Table 2.3: Function mappings for bandpass frequency transform

$\boldsymbol{\Omega}$	$-\infty$	-1	0	1	∞
$\boldsymbol{\omega}$	$-\infty, 0$	$-\omega_2, \omega_1$	$\pm\omega_0$	$-\omega_1, \omega_2$	$0, \infty$

2.3.4 Ideal bandstop filter response

An ideal bandstop filter with a desired stopband bound by lower corner frequency, ω_1, and upper corner frequency, ω_2, with centre frequency, $\omega_0 = \sqrt{\omega_2\omega_1}$, can be obtained by applying the frequency transformation specified by equation 2.3.6 which is the inverse of the bandpass transform and has multiple mappings to the same prototype value [10, 20].

$$\Omega \leftarrow -\Delta \left(\frac{\omega}{\omega_0} - \frac{\omega_0}{\omega} \right)^{-1} \tag{2.3.6}$$

The definition of fractional bandwidth, Δ, is the same as that in equation 2.3.5 for the bandpass case. The resulting bandstop response is illustrated in figure 2.7 with the function mappings illustrated in table 2.4. The same bandstop response could be achieved by a separate highpass filter with $\omega_c = \omega_2$ connected in a shunt-shunt configuration with a lowpass filter with $\omega_c = \omega_1$.

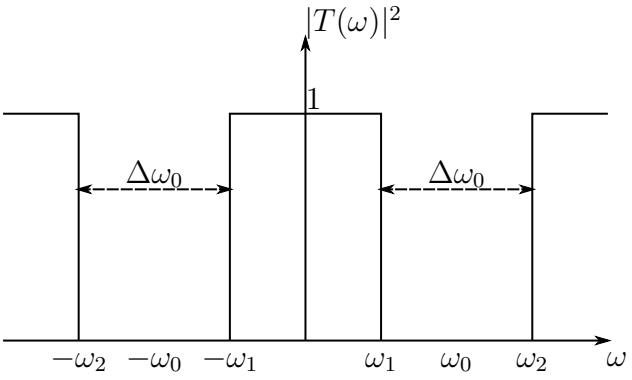

Figure 2.7: Ideal bandstop filter response

Table 2.4: Function mappings for bandstop frequency transform

$\boldsymbol{\Omega}$	$-\infty$	-1	0	1	∞
$\boldsymbol{\omega}$	$\pm\omega_0$	$-\omega_1, \omega_2$	$0, \pm\infty$	$-\omega_2, \omega_1$	$\pm\omega_0$

2.4 Practical approximations of the ideal lowpass prototype response

The ideal prototype response discussed in section 2.3 is not physically realisable as it has a non-causal impulse response in the time domain. In order to overcome this, the ideal prototype response can be approximated by the Butterworth and Chebyshev prototype responses which both have causal impulse responses [16, 21]. Filter responses based on these approximations in particular are all-pole filters.

2.4.1 The Butterworth lowpass approximation

The Butterworth lowpass magnitude approximation has a maximally flat characteristic with a 3dB attenuation at the cut-off frequency with a prototype function specified by

$$P_{\text{LR}} = \frac{1}{|T(\Omega)|^2} = 1 + \Omega^{2N}, \tag{2.4.1}$$

where Ω is the normalised frequency variable and N is the order of the filter [10, 19]. The maximally flat characteristic stems from the fact that the first $2N - 1$ derivatives of Ω^{2N} are zero at $\Omega = 0$ [21]. The main advantage of the Butterworth response is its mathematical simplicity [19].

When $\Omega >> 1$, the stopband insertion loss can be approximated as

$$\begin{aligned} \text{IL} &\approx 10\log(\Omega^{2N}) \\ &\approx 20N\log(\Omega), \end{aligned} \tag{2.4.2}$$

which describes an increase at a rate of 20NdB/decade [21].

Figure 2.8 shows transmission coefficient versus frequency plots for Butterworth prototype responses of different orders [10, 19].

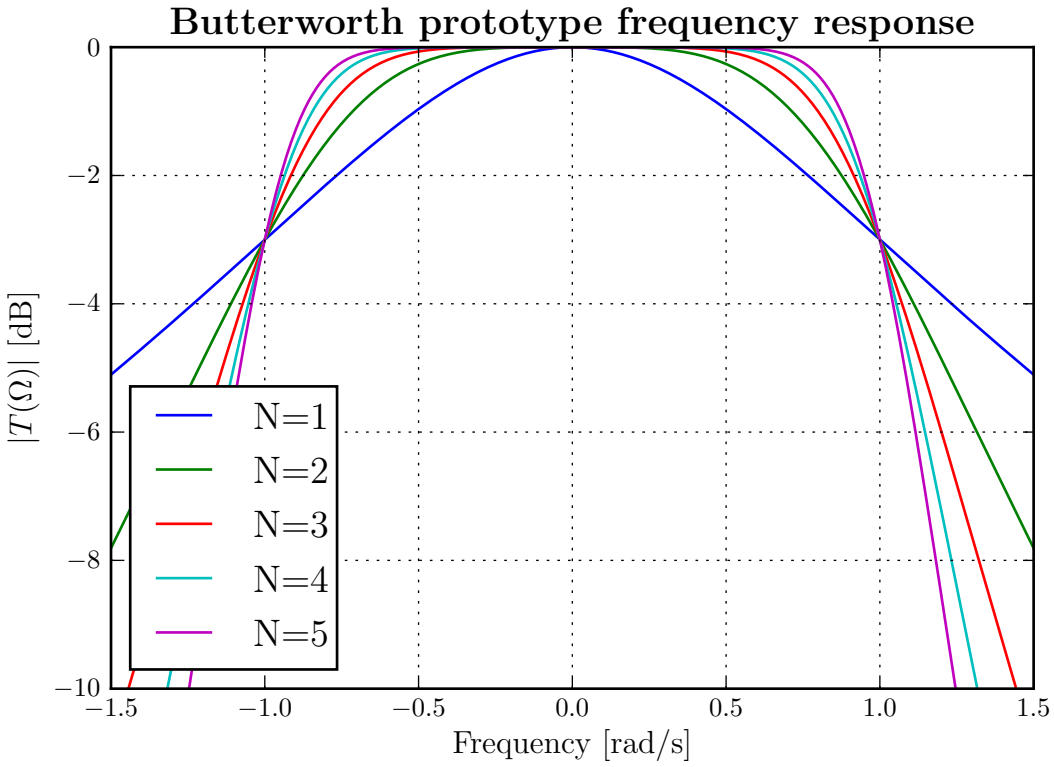

Figure 2.8: Butterworth prototype responses for $N \in [1, 5]$

From the plots in figure 2.8, the gradient of the roll-off slope depicting the transition between the passband and stopband increases as N increases which results in more flatness in the passband and greater attenuation in the stopband [9]. The main disadvantage of the Butterworth response is that the passband transmission characteristic is not uniform across frequencies and for small values of N the stopband attenuation is not adequate enough for high demanding filtering requirements [19, 21].

2.4.2 The Chebyshev lowpass approximation

The Chebyshev lowpass magnitude response has an equal-ripple characteristic in the passband with a prototype function specified by:

$$P_{\text{LR}} = \frac{1}{|T(\Omega)|^2} = 1 + \epsilon^2 C_N^2(\Omega) \tag{2.4.3}$$

and

$$\epsilon = \sqrt{10^{\frac{R_{\text{dB}}}{10}} - 1}, \tag{2.4.4}$$

where $C_N(\Omega)$ is the Chebyshev polynomial function, Ω is the normalised frequency variable, N is the order of the filter and R_{dB} determines the ripple factor and attenuation at the cut-off frequency [19]. The equal-ripple characteristic stems from the Chebyshev polynomial function specified by equation 2.4.5.

$$C_N(\Omega) = \begin{cases} \cos(N\cos^{-1}(\Omega)) & |\Omega| \leq 1 \\ \cosh(N\cosh^{-1}(\Omega)) & |\Omega| \geq 1 \end{cases} \tag{2.4.5}$$

When $\Omega >> 1$, the stopband insertion loss can be approximated as

$$\begin{aligned} \text{IL} &\approx 10\log(\epsilon^2(2^{N-1}\Omega^N)^2) \\ &\approx 20\log(\epsilon) + 20(N-1)\log(2) + 20N\log(\Omega) \\ &\approx 20\log(\epsilon) + 6(N-1) + 20N\log(\Omega), \end{aligned} \tag{2.4.6}$$

which depending on ϵ and N can increase at a rate greater than or less than $20N$dB/decade [21].

Figures 2.9 and 2.10 show transmission coefficient versus frequency plots for Chebyshev prototype responses of different orders and ripple factors [10, 19].

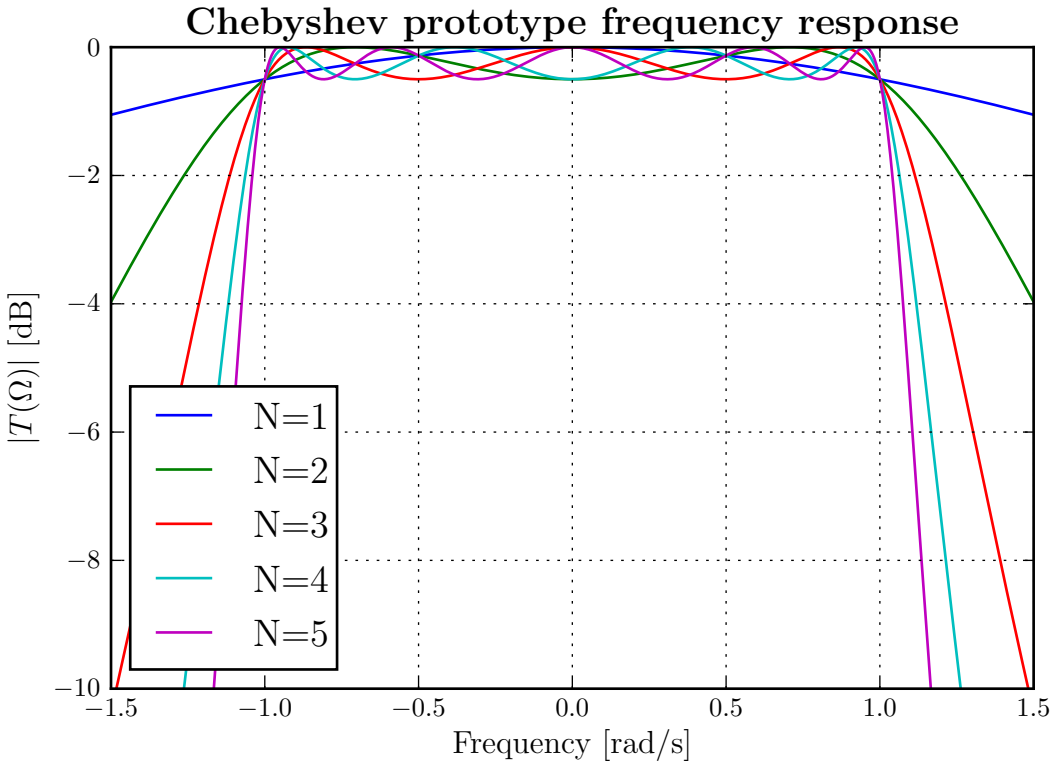

Figure 2.9: Chebyshev (0.5dB ripple) prototype responses for $N \in [1, 5]$

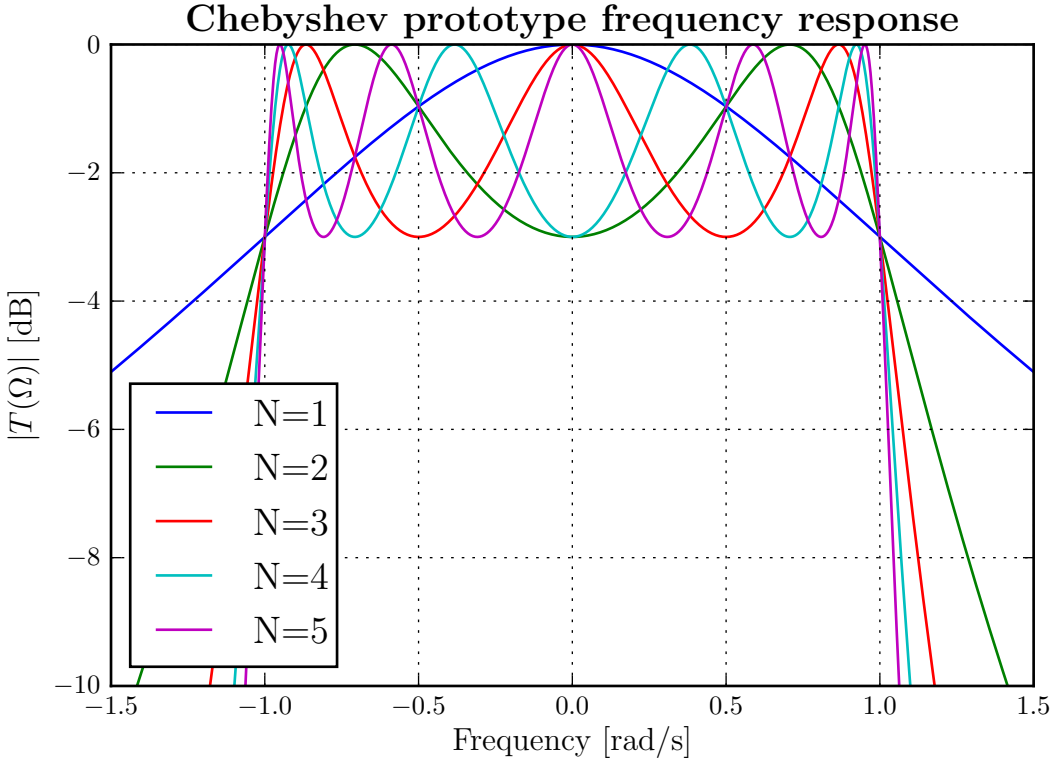

Figure 2.10: Chebyshev (3.0dB ripple) prototype responses for $N \in [1, 5]$

From the plots in figures 2.9 and 2.10, as with the Butterworth case, the gradient of the roll-off slope depicting the transition between the passband and stopband increases as N and ϵ increase which is evident from equation 2.4.6. A comparison of the approximate stopband attenuation for the different prototype responses based on equations 2.4.2 and 2.4.6, where $\Omega >> 1$, is presented in table 2.5.

Table 2.5: Comparison of approximate stopband ($\Omega >> 1$) insertion loss for different prototype responses

N	**Butterworth**	**Chebyshev (0.5dB ripple)**	**Chebyshev (3.0dB ripple)**
1	20dB/decade	-9dB + 20dB/decade	20dB/decade
2	40dB/decade	-3dB + 40dB/decade	6dB + 40dB/decade
3	60dB/decade	3dB + 60dB/decade	12dB + 60dB/decade
4	80dB/decade	9dB + 80dB/decade	18dB + 80dB/decade
5	100dB/decade	15dB + 100dB/decade	24dB + 100dB/decade

One of the advantages that the Chebyshev response presents over the Butterworth response is that ϵ introduces an additional degree of freedom for greater control over the passband and stopband characteristics. The passband insertion loss can be minimised to better approximate the ideal filter behaviour by choosing small values for ϵ. From the comparison in table 2.5, it is clear that the Chebyshev (3.0dB ripple) has the best stopband performance out of the group. The Chebyshev (0.5dB ripple) has the best passband performance with a stopband performance exceeding that of the Butterworth when $N \geq 3$. Overall, the selectivity of the Chebyshev response makes it a superior choice above the Butterworth response to satisfy high demanding filtering requirements [21]. The main disadvantage of the Chebyshev response is that it is more mathematically complex than the Butterworth response and has a ripple present in its passband. The Chebyshev response in general has a poor group delay response as a consequence of its strong selectivity characteristics [9, 19].

2.5 Fixed frequency notch filter response

An ideal narrowband bandstop filter response can be approximated by applying the frequency transformation specified by equation 2.3.6 to the Butterworth and Chebyshev prototype functions. The definitions of the bandstop frequency transformation and fractional bandwidth are repeated below.

$$\Omega \leftarrow -\Delta \left(\frac{\omega}{\omega_0} - \frac{\omega_0}{\omega} \right)^{-1}$$

$$\Delta = \frac{\omega_2 - \omega_1}{\omega_0}$$

For a narrowband bandstop response where the centre frequency is of greater importance to specify than the corner frequencies, the fractional bandwidth can be expressed alternatively as

$$\begin{aligned} \Delta &= \frac{\omega_2 - \omega_1}{\omega_0} \\ &= \frac{\omega_{\text{BW}}}{\omega_0} \qquad (2.5.1a) \\ &= \frac{f_{\text{BW}}}{f_0} \qquad (2.5.1b) \end{aligned}$$

where f_{BW} is the absolute bandwidth of the notch between the corner frequencies [16]. With the filter specifications taken into account, the centre frequency is chosen as $f_0 = 445\text{MHz}$ with the absolute bandwidth of the notch chosen as $f_{\text{BW}} = 4.45\text{MHz}$ such that $\Delta = 0.01$ for a narrowband implementation.

Figures 2.11-2.13 show transmission coefficient versus frequency plots for Butterworth, Chebyshev (0.5dB ripple) and Chebyshev (3.0dB ripple) notch filter responses of different orders respectively.

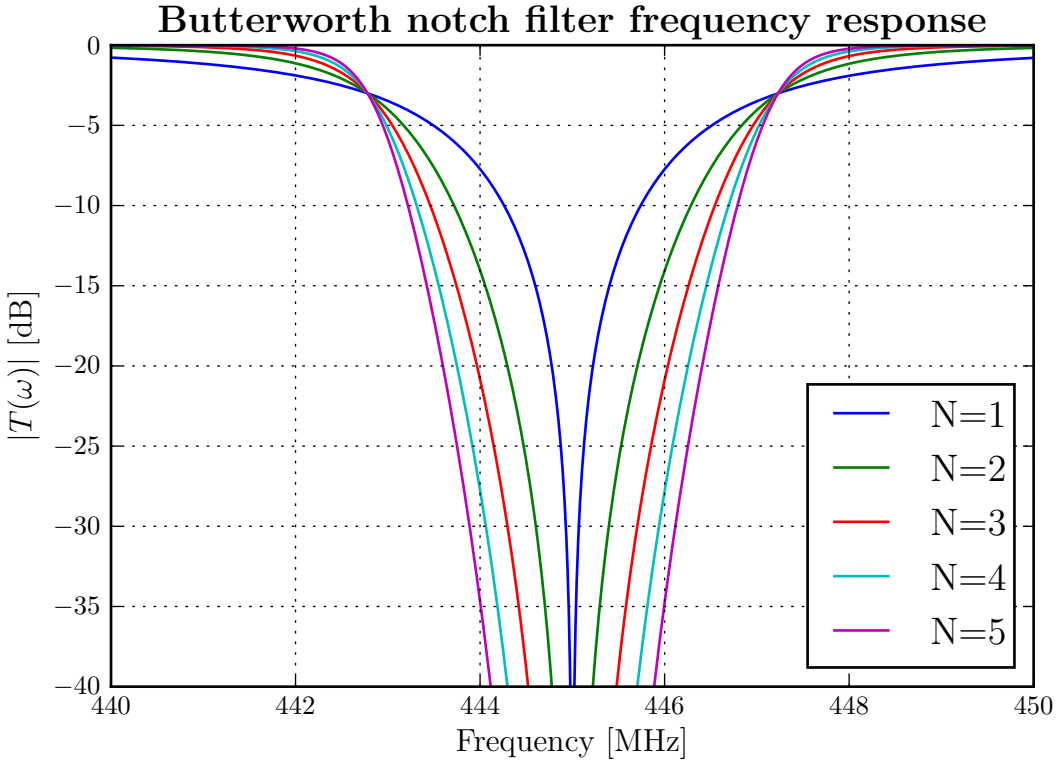

Figure 2.11: Butterworth notch filter response for $N \in [1, 5]$

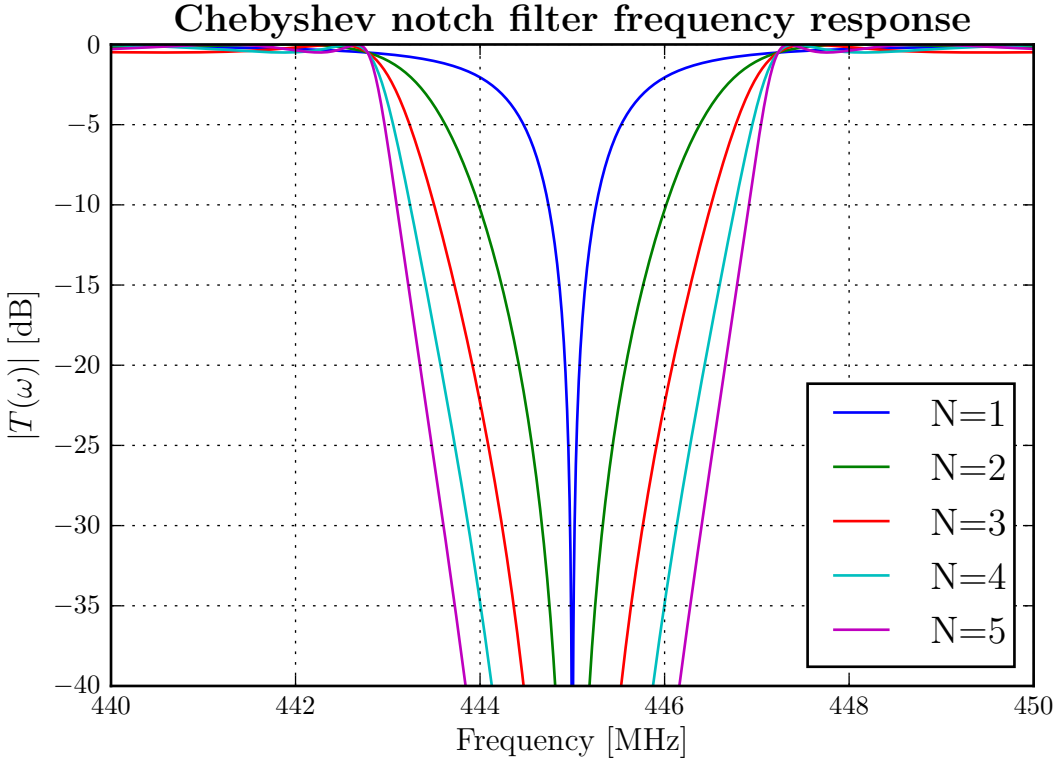

Figure 2.12: Chebyshev (0.5dB ripple) notch filter response for $N \in [1, 5]$

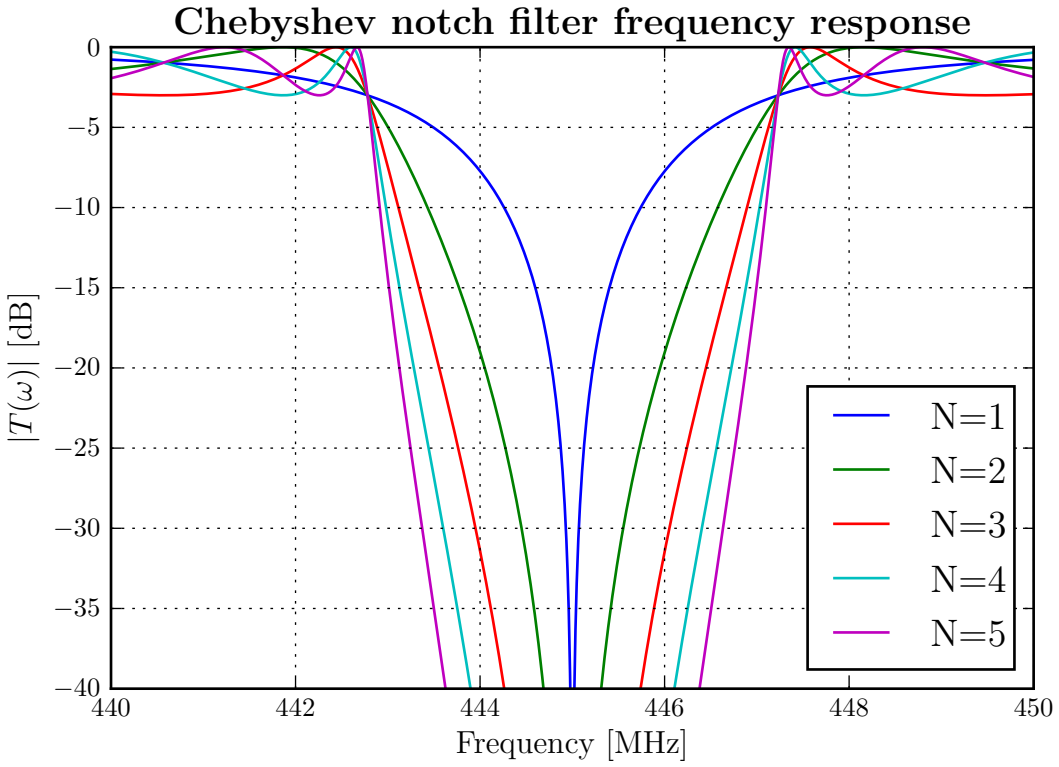

Figure 2.13: Chebyshev (3.0dB ripple) notch filter response for $N \in [1, 5]$

From the plots in figures 2.11-2.13, the same passband and stopband attributes are inherited from the respective prototype of each response type. The attenuation of the notch at the centre frequency is infinite for all values of N.

The filter is required to only attenuate the frequencies within the unwanted band at a given time whilst all other frequencies need to pass through undistorted. The primary requirement is ensuring that the notch bandwidth at the 40dB attenuation mark, $\omega_{40\text{dB}}$, is sufficient to suppress an entire radio channel. A secondary requirement will be to maximise the passband for detection of signals outside of the notch. A comparison of the ratio between the 40dB, $\omega_{40\text{dB}}$, and 3dB, $\omega_{3\text{dB}}$, notch bandwidths for the different filter responses is presented in figure 2.14.

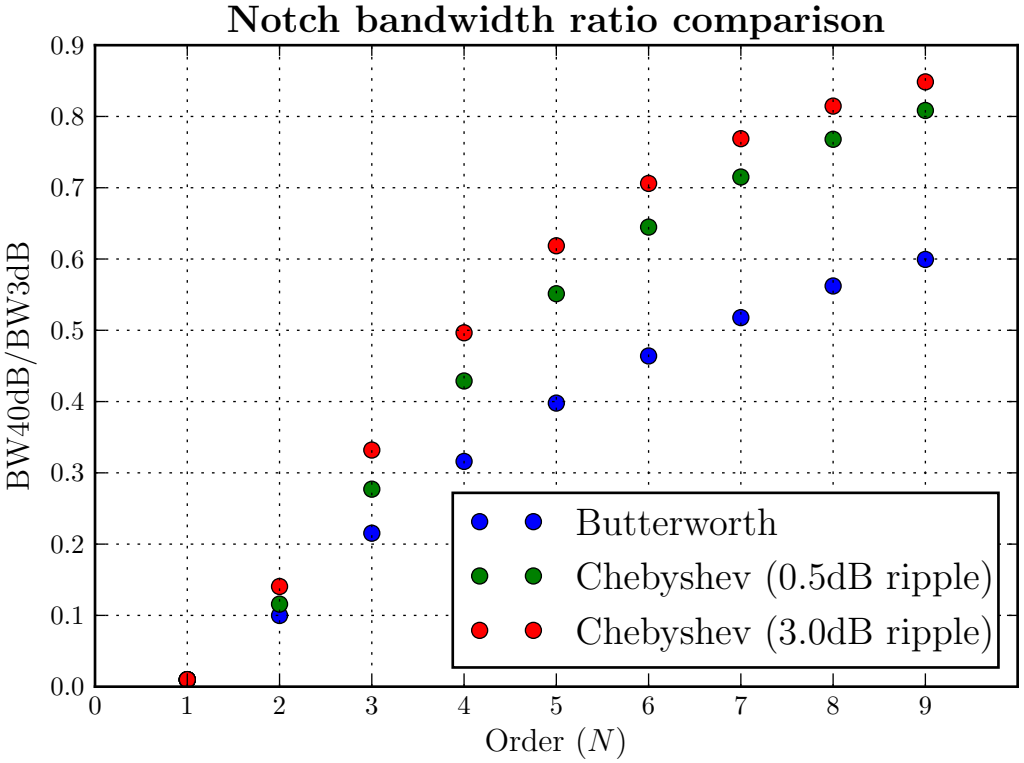

Figure 2.14: Notch bandwidth ratio comparison for Chebyshev and Butterworth responses

Based on the plot in figure 2.14, the Chebyshev (3.0dB ripple) response clearly exhibits the most superior stopband performance above all the other responses. To keep the design simple with minimal reactive components, the order N is chosen as 3. At $N = 3$, the Chebyshev (0.5dB ripple) response has stopband performance above the Butterworth response and does not sacrifice too much performance in the passband in comparison to the Chebyshev (3.0dB ripple) response. The best compromise is reached by choosing the Chebyshev (0.5dB ripple) response.

2.6 Immittance inverters

An ideal immittance inverter is a two-port network that behaves like a quarter-wave transformer at all frequencies [22]. The term immittance inverter is a generic term that refers to both impedance and admittance inverters as they are the exact same network with the distinction that they are defined in different units [16]. Figure 2.15 shows a block representation of an ideal impedance inverter terminated with a load impedance at port 2. The input impedance at port 1 is related to the load impedance by

$$Z_{\text{in}} = \frac{K^2}{Z_{\text{L}}}, \tag{2.6.1}$$

where K is the inverter constant in Ohms used to define the inverter [22]. An impedance inverter thus inverts the load impedance and scales it by a factor of K^2. The same equation is valid to determine the input impedance at port 2 if port 1 is terminated with a load impedance.

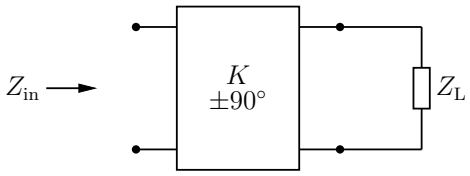

Figure 2.15: Block representation of impedance inverter circuit

The input impedance relation in equation 2.6.1 is identical to that of a quarter-wave transformer with a characteristic impedance of K terminated with a load impedance at port 2. Equation 2.6.1 does not take the $\pm 90°$ phase shift into account. A complete description of the working of an impedance inverter is given by its transmission matrix, $\mathbf{T}_{\text{K}}$ [16].

$$\left[\mathbf{T}_{\text{K}}\right] = \begin{bmatrix} 0 & \pm jK \\ \mp 1/jK & 0 \end{bmatrix} \tag{2.6.2}$$

An ideal impedance inverter can be implemented as a T-network with frequency independent reactances specified by $K = |X|$ shown in figure 2.16 [23].

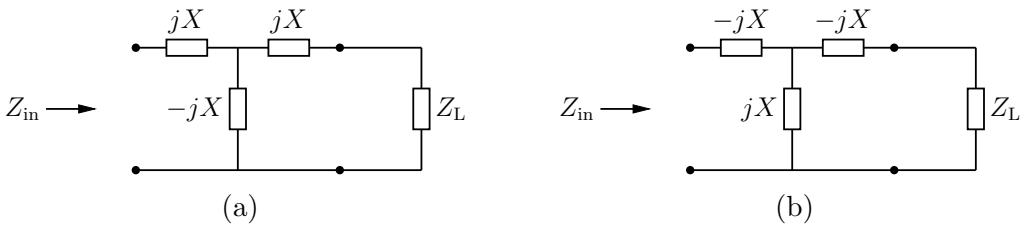

Figure 2.16: T-model representations of impedance inverter circuit. (a) Configuration for a $+90°$ phase shift. (b) Configuration for a $-90°$ phase shift.

The admittance inverter is the same network as the impedance inverter, but the elements are expressed as admittances rather than impedances. Figure 2.17 shows a block representation of an ideal admittance inverter terminated with a load admittance at port 2. The input admittance at port 1 is related to the load admittance by

$$Y_{\text{in}} = \frac{J^2}{Y_{\text{L}}} \tag{2.6.3}$$

where J is the inverter constant in Siemens used to define the inverter [22].

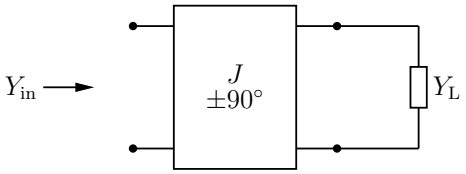

Figure 2.17: Block representation of admittance inverter circuit

The admittance inverter is related to the impedance inverter by $J = 1/K$ and is described by the transmission matrix, $\mathbf{T}_{\text{J}}$ [16].

$$\left[\mathbf{T}_{\text{J}}\right] = \begin{bmatrix} 0 & \pm 1/jJ \\ \mp jJ & 0 \end{bmatrix} \tag{2.6.4}$$

An ideal admittance inverter can be implemented as a pi-network with frequency independent suscpetances specified by $J = |B|$ shown in figure 2.18 [23].

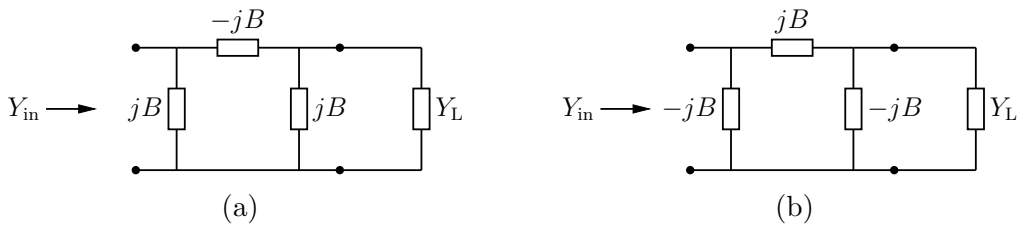

Figure 2.18: Pi-model representations of admittance inverter circuit. (a) Configuration for a $+90°$ phase shift. (b) Configuration for a $-90°$ phase shift.

A shunt element within a network described by transmission matrix, $\mathbf{T}_{\mathrm{Y}}$, is shown in figure 2.19a and can be transformed into a series element with an inverter on either side described by transmission matrix, $\mathbf{T}_{\mathrm{KZK}}$, shown in figure 2.19b.

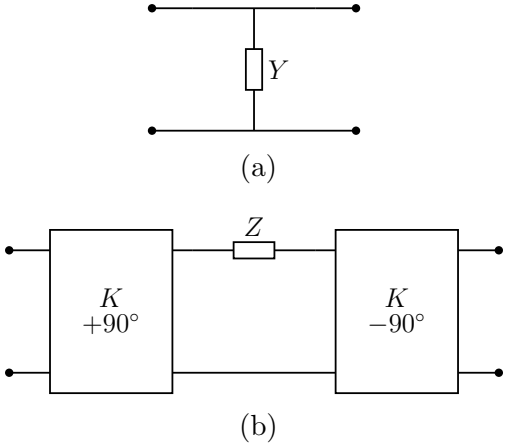

Figure 2.19: (a) Network with a shunt admittance. (b) Equivalent network with a series impedance and impedance inverters.

$$\left[\mathbf{T}_{\mathrm{Y}}\right] = \begin{bmatrix} 1 & 0 \\ Y & 1 \end{bmatrix} \tag{2.6.5}$$

$$\left[\mathbf{T}_{\mathrm{KZK}}\right] = \begin{bmatrix} 0 & jK \\ j/K & 0 \end{bmatrix} \begin{bmatrix} 1 & Z \\ 0 & 1 \end{bmatrix} \begin{bmatrix} 0 & -jK \\ -j/K & 0 \end{bmatrix} \tag{2.6.6}$$

$$= \begin{bmatrix} 1 & 0 \\ Z/K^2 & 1 \end{bmatrix} \tag{2.6.7}$$

Equating equations 2.6.5 and 2.6.7 shows that the shunt element in figure 2.19a is related to the series element and inverters in figure 2.19b by

$$Y = \frac{Z}{K^2}. \tag{2.6.8}$$

If the inverters are chosen to have identical phase characteristics then a phase shift of $\pm 180°$ will be introduced into the transmission path.

In a similar manner, a series element within a network described by transmission matrix, $\mathbf{T}_{\mathrm{Z}}$, is shown in figure 2.20a and can be transformed into a shunt element with an inverter on either side described by transmission matrix, $\mathbf{T}_{\mathrm{JYJ}}$, shown in figure 2.20b.

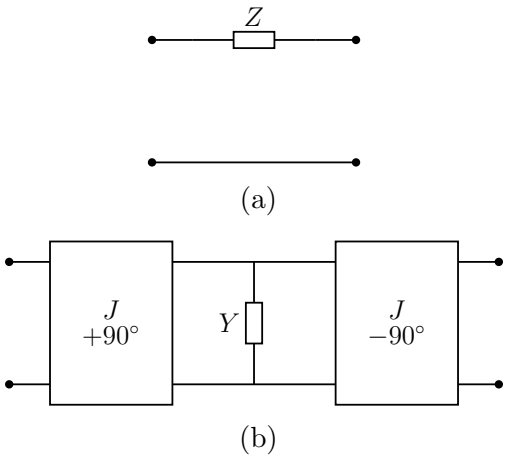

Figure 2.20: (a) Network with a series impedance. (b) Equivalent network with a shunt admittance and admittance inverters.

$$\left[\mathbf{T}_{\mathrm{Z}}\right] = \begin{bmatrix} 1 & Z \\ 0 & 1 \end{bmatrix} \tag{2.6.9}$$

$$\begin{aligned} \left[\mathbf{T}_{\mathrm{JYJ}}\right] &= \begin{bmatrix} 0 & j/J \\ jJ & 0 \end{bmatrix} \begin{bmatrix} 1 & 0 \\ Y & 1 \end{bmatrix} \begin{bmatrix} 0 & -j/J \\ -jJ & 0 \end{bmatrix} \\ &= \begin{bmatrix} 1 & Y/J^2 \\ 0 & 1 \end{bmatrix} \end{aligned} \tag{2.6.10}$$

Equating equations 2.6.9 and 2.6.10 shows that the series element in figure 2.20a is related to the shunt element and inverters in figure 2.20b by

$$Z = \frac{Y}{J^2}. \tag{2.6.11}$$

2.7 The Q-factor of resonant circuits

Resonators play a vital role in the implementation of a desired filter response in circuitry due to their frequency selective behaviour. This behaviour is based on their properties to sustain electromagnetic field oscillations at specific frequencies [20].

A lossy lumped element series resonator can be modelled by the RLC circuit shown in figure 2.21 with an input impedance described by equation 2.7.1 [10]. The loss in the resonator is represented by the parasitic resistor, R_{p}.

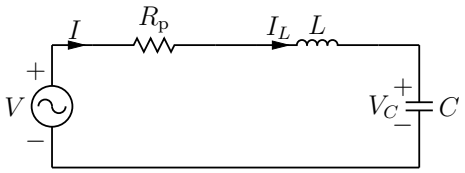

Figure 2.21: Series RLC resonator circuit

$$Z_{\mathrm{in}} = R_{\mathrm{p}} + j\omega L - \frac{j}{\omega C} \tag{2.7.1}$$

The total time average complex power delivered to the resonator is

$$P = \frac{1}{2} V I^* = \frac{1}{2} |I|^2 Z_{\mathrm{in}}, \tag{2.7.2}$$

where the real component of the complex power described by equation 2.7.2 is the loss in the resonator which can be expressed separately as

$$P_{\mathrm{loss}} = \frac{1}{2} |I|^2 R_{\mathrm{p}}. \tag{2.7.3}$$

The average magnetic and electric energy stored in the resonator due to the current through inductor L and voltage across capacitor C is

$$W_{\mathrm{m}} = \frac{1}{4} |I|^2 L \tag{2.7.4}$$

and

$$W_{\mathrm{e}} = \frac{1}{4} |V_c|^2 C = \frac{1}{4} |I|^2 \frac{1}{\omega^2 C} \tag{2.7.5}$$

respectively [10, 20].

Resonance occurs when the average magnetic and electric energies stored in the resonator are equal [20]. By equating equations 2.7.4 and 2.7.5, the frequency at which resonance occurs can be solved for in terms of the values of the inductor L and capacitor C to yield

$$\omega_0 = \frac{1}{\sqrt{LC}}. \tag{2.7.6}$$

The expression for the input impedance described by equation 2.7.1 can be expressed in terms of the resonant frequency through substitution of equation 2.7.6 to yield

$$\begin{aligned} Z_{\text{in}} &= R_{\text{p}} + j\omega L\left(1 - \frac{1}{\omega^2 LC}\right) \\ &= R_{\text{p}} + j\omega L\left(1 - \frac{\omega_0^2}{\omega^2}\right) \\ &= R_{\text{p}} + j\omega L\left(\frac{\omega^2 - \omega_0^2}{\omega^2}\right), \end{aligned} \tag{2.7.7}$$

from which it can be shown that $\text{Im}(Z_{\text{in}}) = X = 0$ at resonance.

The quality factor or Q-factor is a figure of merit used to measure the energy efficiency of a resonator and is defined as

$$\begin{aligned} Q &= \omega\frac{\text{average energy stored}}{\text{energy loss/second}} \\ &= \omega\frac{W_{\text{m}} + W_{\text{e}}}{P_{\text{loss}}}. \end{aligned} \tag{2.7.8}$$

The Q-factor defined here is strictly the unloaded Q-factor that only accounts for the loss within the resonator itself and does not take the effect of loading into account when an external resistance is connected in series with the resonator [10]. The Q-factor is evaluated at resonance such that $W_{\text{m}} = W_{\text{e}}$ to yield

$$\begin{aligned} Q_0 &= \omega_0\frac{2W_{\text{m}}}{P_{\text{loss}}} \\ &= \frac{\omega_0 L}{R_{\text{p}}} && \text{(2.7.9a)} \\ &= \frac{1}{\omega_0 C R_{\text{p}}} && \text{(2.7.9b)} \end{aligned}$$

which conveniently describes the Q-factor at resonance in terms of the parasitic resistance R_{p}, resonant frequency ω_0 and either the value of inductor L or capacitor C. From equations 2.7.9a and 2.7.9b it is evident that the Q-factor decreases as R_{p} increases.

A lossy resonator can be modelled by a lossless resonator with a complex resonant frequency by applying the following transform [10]:

$$\omega_0' \rightarrow \omega_0 \left(1 + \frac{j}{2Q_0}\right). \tag{2.7.10}$$

A basic derivation for the transform described by equation 2.7.10 shall now be presented. For frequencies near the resonant frequency such that $\omega = \omega_0 + \Delta\omega$ or $\omega_0 = \omega - \Delta\omega$, where $\Delta\omega$ is small, equation 2.7.7 can be rewritten as

$$\begin{aligned} Z_{\text{in}} &= R_{\text{p}} + j\omega L \left(\frac{\omega^2 - (\omega^2 - 2\omega\Delta\omega + \Delta\omega^2)}{\omega^2}\right) \\ &= R_{\text{p}} + j\omega L \left(\frac{2\omega\Delta\omega - \Delta\omega^2}{\omega^2}\right). \end{aligned} \tag{2.7.11}$$

Equation 2.7.11 can be reduced by neglecting the $\Delta\omega^2$ term and substituting equation 2.7.9a to yield

$$\begin{aligned} Z_{\text{in}} &\approx R_{\text{p}} + j\omega L \left(\frac{2\omega\Delta\omega}{\omega^2}\right) \\ &\approx R_{\text{p}} + j2L\Delta\omega \\ &\approx R_{\text{p}} + j2Q_0R_{\text{p}} \left(\frac{\Delta\omega}{\omega_0}\right), \end{aligned} \tag{2.7.12}$$

which approximates the input impedance of the resonator in terms of the Q-factor for frequencies close to the resonant frequency.

For a lossless resonator, where $R_{\text{p}} = 0$, equation 2.7.12 can be simplified to

$$\begin{aligned} Z_{\text{in}} &\approx j2L\Delta\omega \\ &\approx j2L(\omega - \omega_0). \end{aligned} \tag{2.7.13}$$

By equating equations 2.7.12 and 2.7.13, the lossy model is related to the lossless model and the frequency transform can be extracted as follows:

$$\begin{aligned} j2L(\omega - \omega_0') &= R_\mathrm{p} + j2Q_0R_\mathrm{p}\left(\frac{\Delta\omega}{\omega_0}\right) \\ \omega - \omega_0' &= \frac{R_\mathrm{p}}{j2L} + \frac{Q_0R_\mathrm{p}}{L}\left(\frac{\Delta\omega}{\omega_0}\right) \\ \omega_0' &= \omega - \frac{R_\mathrm{p}}{j2L} - \Delta\omega \\ \omega_0' &= \omega - \frac{\omega_0}{j2Q_0} - \omega + \omega_0 \\ \omega_0' &= \omega_0\left(1 + \frac{j}{2Q_0}\right). \end{aligned}$$

A lossy lumped element parallel resonator can be modelled by the RLC circuit shown in figure 2.22. Just like the case with the series resonator, the parasitic resistor, R_p, represents loss in the resonator.

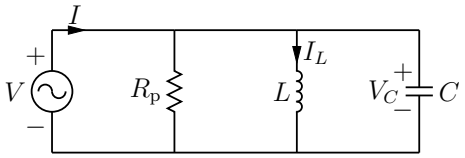

Figure 2.22: Parallel RLC resonator circuit

In a similar manner to the series resonator case, it can be shown that the unloaded Q-factor at resonance for a parallel resonator is

$$\begin{aligned} Q_0 &= \omega_0\frac{2W_\mathrm{m}}{P_\mathrm{loss}} \\ &= \frac{R_\mathrm{p}}{\omega_0 L} && \text{(2.7.14a)} \\ &= \omega_0 C R_\mathrm{p}, && \text{(2.7.14b)} \end{aligned}$$

which is the inverse of the unloaded Q-factor of a series resonator [20].

A lossy parallel resonator can also be modelled as lossless parallel resonator by applying the frequency transform described by equation 2.7.10 [10].

2.8 Filter circuit model

Up to this point, the mathematical descriptions of the Butterworth and Chebyshev filter responses have been discussed in detail. This section will show how either of these filter responses can be implemented in circuitry using inductors and capacitors through application of ladder synthesis [16]. The principle of ladder synthesis is to extract the input impedance function, $Z_{\text{in}}(\Omega)$, from the desired prototype transfer function, $T(\Omega)$, in order to relate the mathematical description of the filter response to a physical circuit model.

2.8.1 Prototype lumped-element ladder network

Two generalised lowpass filter configurations are shown in figures 2.23 and 2.24. These configurations are referred to as duals of one another as they produce the same response for a given set of normalised component values, g_0 - $g_{\text{n}+1}$, related to the circuit elements by equations 2.8.1 - 2.8.3 [20]. The normalised component values corresponding to Butterworth and Chebyshev prototypes for different orders, N, are readily available from filter tables presented in [22] and can be utilised without the need to be calculated from first principles.

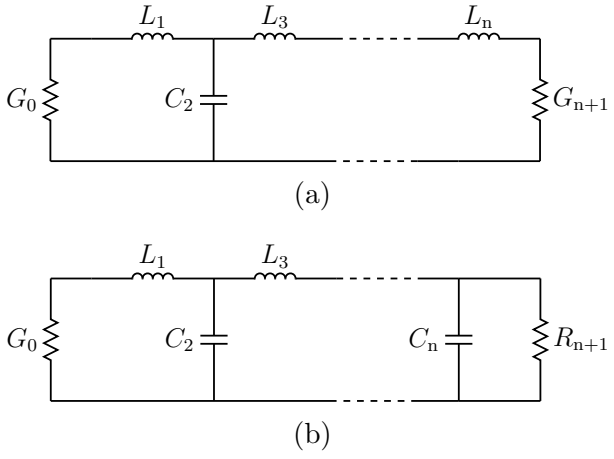

Figure 2.23: Prototype ladder networks in type 1 Cauer topology for: (a) N odd; and (b) N even.

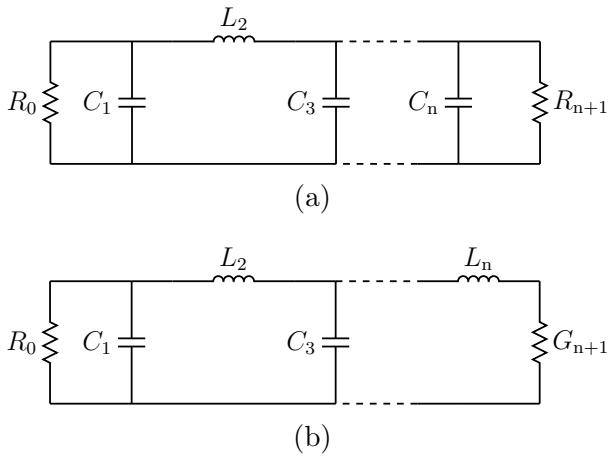

Figure 2.24: Prototype ladder networks in type 2 Cauer topology for: (a) N odd; and (b) N even.

$$g_0 = R_0 = G_0 \tag{2.8.1}$$

$$g_k = C_k = L_k \tag{2.8.2}$$

$$g_{n+1} = R_{n+1} = G_{n+1} \tag{2.8.3}$$

The main disadvantage of implementing a filter response using the ladder networks is that the component values cannot be chosen independently and the networks can only be symmetrical for odd values of N. Even order Chebyshev responses in particular do not yield a circuit with identical terminating impedances and matching networks would be required [16].

2.8.2 Prototype circuit model with shunt capacitors and admittance inverters

The shortcomings of the ladder networks discussed in section 2.8.1 can be resolved with the aid of immittance inverters. Figure 2.25a shows an arbitrary middle segment of a nth order ladder network with normalised component values. If the network is denormalised and the value of the capacitor is chosen as C_{ak} shown in figure 2.25b, then the rest of the entire network has to be impedance scaled by a factor of C_k/C_{ak} to ensure that the filter response stays the same. This is an example of the limitations that the ladder networks present when component values need to be chosen independently. By recognising that the inductor is a series component, it can be transformed into a shunt capacitor with adjacent inverters shown in figure 2.26. By assuming that both inverters are identical and applying

equation 2.6.11, the inductor is related to the capacitor and inverters as follows:

$$j\omega L_{k+1}(C_k/C_{ak}) = \frac{j\omega C_{a(k+1)}}{J^2_{kk+1}}. \tag{2.8.4}$$

The value of the inverter constant can be solved by rearranging equation 2.8.4 to yield

$$\begin{aligned} J_{kk+1} &= \sqrt{\frac{C_{ak}C_{a(k+1)}}{C_k L_{k+1}}} \\ &= \sqrt{\frac{C_{ak}C_{a(k+1)}}{g_k g_{k+1}}}. \end{aligned} \tag{2.8.5}$$

Figure 2.25: Arbitrary middle segments of ladder network

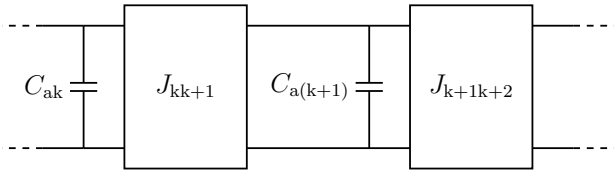

Figure 2.26: Arbitrary middle segment of modified ladder network

Figure 2.27a shows an arbitrary output segment of a nth order ladder network with normalised component values. Similarly, if the network is denormalised and the value of the capacitor is chosen as C_{an} shown in figure 2.27b, then the rest of the entire network has to be impedance scaled by a factor of C_n/C_{an}. By inserting an inverter between the capacitor and terminating impedance shown in figure 2.28, the following equations can be established:

$$R_{n+1}(C_n/C_{an}) = \frac{1}{J^2_{nn+1}R_L} \tag{2.8.6}$$

and

$$J_{\mathrm{nn+1}} = \sqrt{\frac{C_{\mathrm{an}}}{C_{\mathrm{n}} R_{\mathrm{n+1}} R_{\mathrm{L}}}} = \sqrt{\frac{C_{\mathrm{an}}}{g_{\mathrm{n}} g_{\mathrm{n+1}} R_{\mathrm{L}}}}. \tag{2.8.7}$$

Figure 2.27: Output segment of ladder network

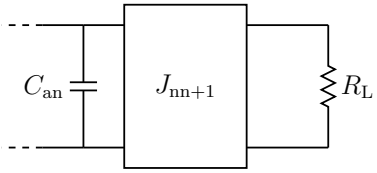

Figure 2.28: Modified output segment of ladder network

In a similar way, the following equations can be established to determine the inverter constant at the input segment:

$$R_0(C_1/C_{\mathrm{a1}}) = \frac{1}{J_{01}^2 R_{\mathrm{S}}} \tag{2.8.8}$$

and

$$J_{01} = \sqrt{\frac{C_{\mathrm{a1}}}{C_1 R_0 R_{\mathrm{S}}}} = \sqrt{\frac{C_{\mathrm{a1}}}{g_0 g_1 R_{\mathrm{S}}}}. \tag{2.8.9}$$

The final modified prototype network with shunt capacitors and admittance inverters is presented in figure 2.29. Apart from potential phase shifts introduced in the transmission path by the inverters, the magnitude response will be unaffected provided that the inverters are ideal. The advantage of this modified network is that it allows the component values and terminating impedances to be chosen independently which offers $N+2$ degrees of freedom as opposed to 1 with a standard ladder network.

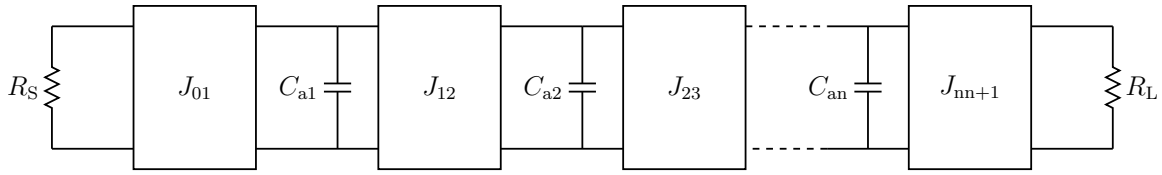

Figure 2.29: Modified prototype network with shunt capacitors and admittance inverters

2.8.3 Fixed frequency notch filter circuit model

The design choice third order Chebyshev (0.5dB ripple) notch filter response was discussed in section 2.4. Recall that the notch was to have a centre frequency of 445MHz and a narrowband fractional bandwidth of $\Delta = 0.01$. The normalised prototype component values required to implement this response using ladder networks are presented in table 2.6 [22].

Table 2.6: Normalised component values for Chebyshev (0.5dB ripple) ladder networks

N	g_0	g_1	g_2	g_3	g_4
3	1.0000	1.5963	1.0967	1.5963	1.0000

The first step is to establish a normalised prototype network of the form in figure 2.29. By choosing all of the capacitor values ($C_{a1} - C_{a3}$) to be equal to $C_1 = g_1$ and the terminating impedances ($R_S - R_L$) to be equal to 1, the inverter constants can be determined using equations 2.8.5, 2.8.7 and 2.8.9 as follows:

$$J_{01n} = 1\text{S},$$
$$J_{12n} = 1.20646\text{S},$$
$$J_{23n} = 1.20646\text{S} = J_{12n},$$
$$J_{34n} = 1\text{S} = J_{01n}.$$

The normalised prototype network corresponding to a third order Chebyshev (0.5dB ripple) response is presented in figure 2.30. It was possible to simplify the network by combining the terminating impedances and end inverters into a single impedance on each side. This simplification will reduce the number of elements required, but will also reduce the degrees of freedom from $N + 2$ to N.

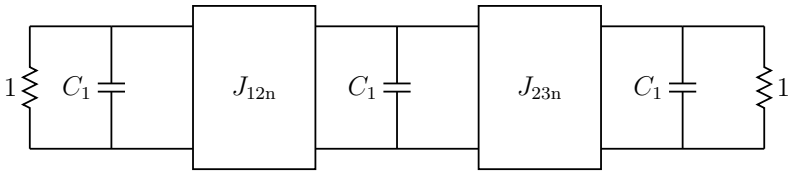

Figure 2.30: Third order Chebyshev (0.5dB ripple) prototype circuit

A lowpass-to-bandstop transform can now be applied to the prototype in figure 2.30. The capacitors are replaced with series LC resonators and the entire circuit is impedance scaled to yield the desired notch filter shown in figure 2.31. The element values are as follows:

$$R_S = R_L = Z_0 = 50\Omega, \tag{2.8.10}$$

$$J_{12} = \frac{J_{12n}}{Z_0} = 24.1292\text{mS}, \tag{2.8.11}$$

$$J_{23} = \frac{J_{23n}}{Z_0} = 24.1292\text{mS}, \tag{2.8.12}$$

$$L_s = \frac{Z_0}{\omega_0 C_1 \Delta} = 1.12025\text{uH}, \tag{2.8.13}$$

$$C_s = \frac{C_1 \Delta}{\omega_0 Z_0} = \frac{1}{\omega_0^2 L_s} = 114.18384\text{fF}. \tag{2.8.14}$$

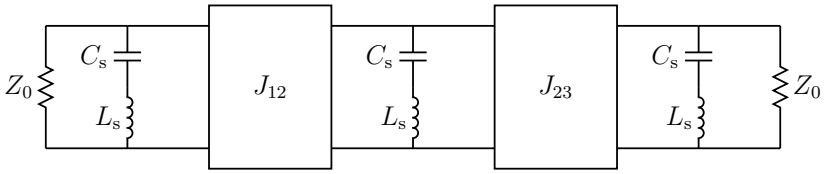

Figure 2.31: Third order Chebyshev (0.5dB ripple) fixed frequency notch filter with series LC resonators

The centre frequency of the notch corresponds to the resonant frequency of the series resonators. Observe that at resonance, the input impedance of the circuit in 2.31 is $Z_{\text{in}}(\omega_0) = 0$ due to the first resonator shorting to ground. The reflection coefficient is

$$\Gamma(\omega_0) = \frac{Z_{\text{in}}(\omega_0) - Z_0}{Z_{\text{in}}(\omega_0) + Z_0} = -1, \tag{2.8.15}$$

which implies that all of the signal power at that frequency is reflected and no transmission occurs.

A major problem with the network presented in figure 2.31 is that the values of the elements in the series resonators are not practical. The value of C_s is too small to be implemented with real capacitors whilst the value of L_s is too large to be implemented with real inductors that can operate faithfully at RF. Additional inverters are incorporated to transform the series LC resonators into parallel LC tank resonators shown in figure 2.32. The additional inverters are chosen to be identical and are denoted as J_r. The new element values of the capacitors and inductors in the parallel LC tank resonators are:

$$L_p = \frac{C_s}{J_r^2} \tag{2.8.16}$$

and

$$C_p = J_r^2 L_p = \frac{1}{\omega_0^2 L_p}. \tag{2.8.17}$$

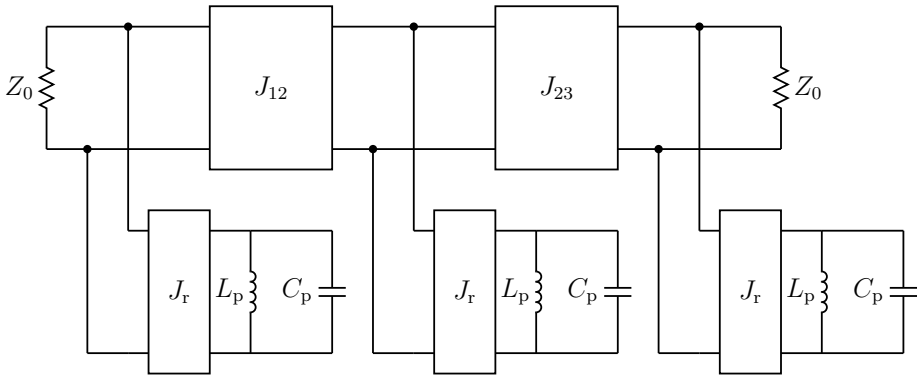

Figure 2.32: Third order Chebyshev (0.5dB ripple) fixed frequency notch filter with parallel LC tank resonators

The introduction of the additional inverters has increased the degrees of freedom in the network from N to $N + 2$ and allows for the parallel LC resonators to be realised with practical components which can be chosen freely.

2.8.4 The impact of lossy resonators on the filter performance

The notch filter model that has been derived up to this point has been implemented with lossless resonators which have an unloaded Q-factor of infinity. This section will investigate the effects that lossy resonators with finite unloaded Q-factors will have on the frequency response of the filter. Due to the fact that the filter circuit model was derived from the mathematical description of the transmission coefficient, the frequency transform that models lossy resonators as lossless resonators with a complex resonant frequency described by equation 2.7.10 can be directly substituted into the transmission coefficient function without the need to perform a simulation with the circuit model. Figure 2.33 shows a plot of the transmission coefficient versus frequency for various values of Q.

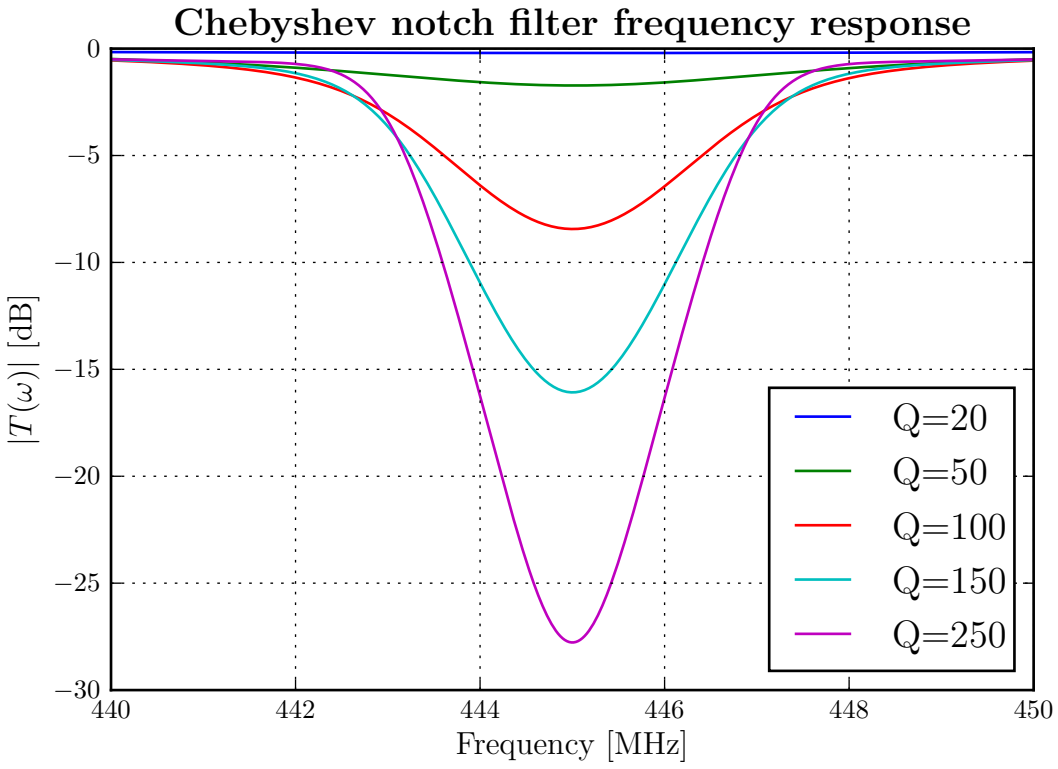

Figure 2.33: Q-factor comparison for 3rd order Chebyshev (0.5dB ripple) notch filter

From the plots in figure 2.33, it can be seen that the attenuation of the notch decreases as the Q factor decreases. For Q-factors as low as 50, the filter response no longer has a visible notch. In order to achieve a notch attenuation of 27.5dB, the Q-factor of the resonators need to be at least 250. Figure 2.34 shows a plot of the notch attenuation at the centre frequency versus fractional bandwidth.

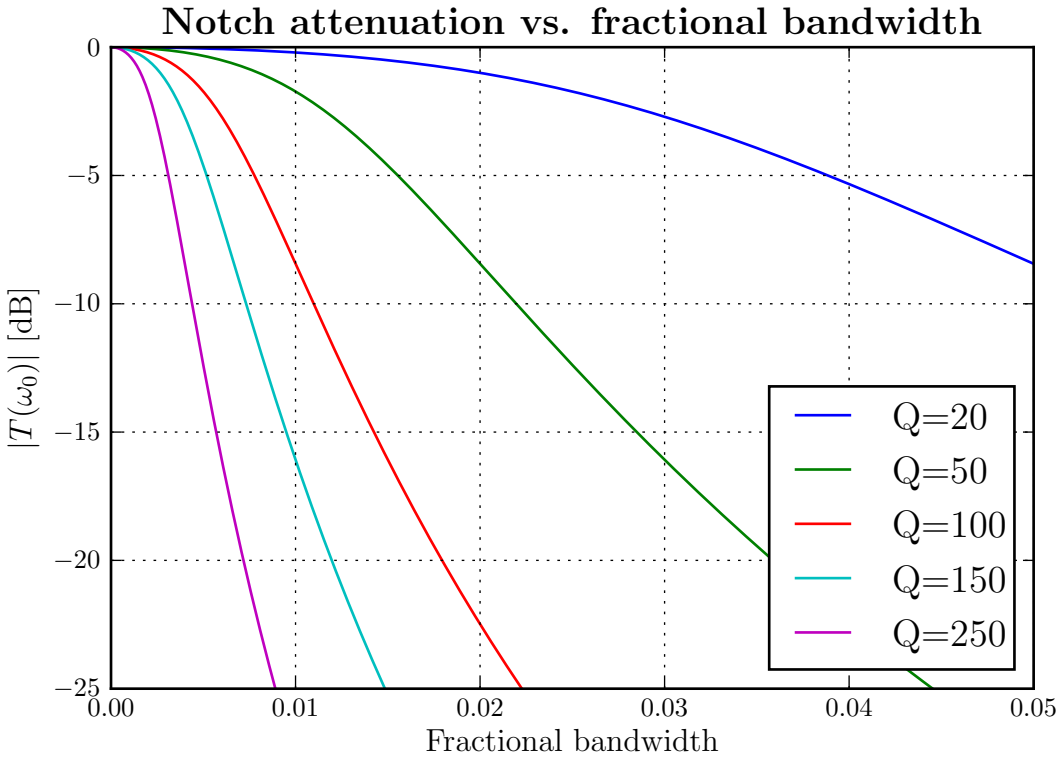

Figure 2.34: Q-factor comparison for 3rd order Chebyshev (0.5dB ripple) notch filter

From the plots in figure 2.34, it can be noted that for a given value of Q, the attenuation at the centre frequency increases as the fractional bandwidth increases. These plots serve as a guideline for what to expect when parameters such as the fractional bandwidth and unloaded Q-factor of the resonators will change with frequency as the position of the notch is varied.

Chapter 3

Practical implementation of filter

An ideal lossless fixed frequency notch filter circuit model was derived at the end of chapter 2. This chapter handles the practical implementation of the filter with non-ideal lumped components and semiconductors. A section is presented on how to model the non-ideal behaviour of components with close attention given to their finite Q-factors. The lossless circuit model is revised to include losses and parasitics. The revised model is simulated in ADS to verify that the desired filter response can still be achieved. The ideal fixed frequency notch filter circuit model is presented again in figure 3.1 with accompanying element values in table 3.1 for convenience.

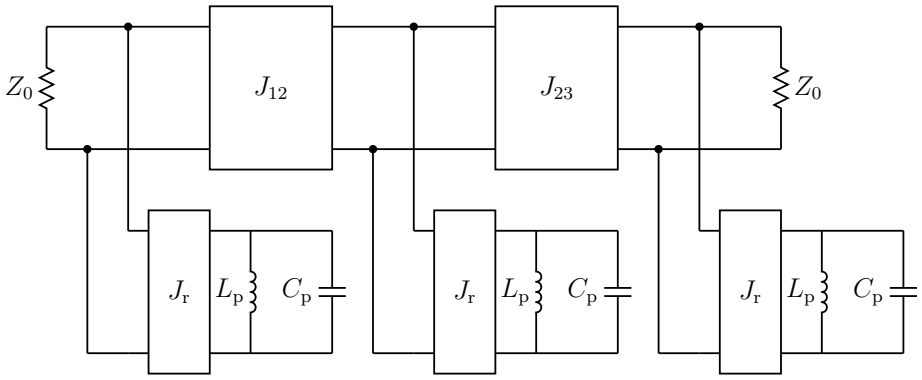

Figure 3.1: Ideal fixed frequency notch filter with parallel LC tank resonators

Table 3.1: Component values for ideal fixed frequency notch filter

J_{12}	J_{23}	L_s	C_s	L_p	C_p
24.1292mS	24.1292mS	1.12025uH	114.18384fF	C_s/J_r^2	$J_r^2 L_s$

3.1 Tuning implementation

As stated in chapter 2, the centre frequency of the notch in the filter's frequency response corresponds to the resonant frequency of the resonators in the circuit model. Recall that $\omega_0 = 1/\sqrt{LC}$ for any resonator (series or parallel). A tunable parallel LC tank circuit is shown in figure 3.2. The inductor, L_p, is kept constant and tuning is achieved by varying the capacitance, C_p, which changes the resonant frequency. The minimum and maximum capacitance values required to tune the filter over the desired frequency range can be determined as follows:

$$C_{\mathrm{p(max)}} = \frac{1}{\omega_{0,\mathrm{L}}^2 L_\mathrm{p}} \tag{3.1.1}$$

and

$$C_{\mathrm{p(min)}} = \frac{1}{\omega_{0,\mathrm{H}}^2 L_\mathrm{p}}, \tag{3.1.2}$$

where $\omega_{0,\mathrm{L}}$ and $\omega_{0,\mathrm{H}}$ are the minimum and maximum desired centre frequencies to tune the notch to.

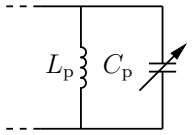

Figure 3.2: Resonator tuning implementation

The effects of tuning on the absolute bandwidth of the notch can be illustrated by expressing L_p in terms of the prototype value and bandstop transformation as follows:

$$L_\mathrm{p} = \frac{C_\mathrm{s}}{J_\mathrm{r}^2} \tag{3.1.3a}$$

$$= \frac{C_1 \Delta}{Z_0 \omega_0 J_\mathrm{r}^2} \tag{3.1.3b}$$

$$= \frac{C_1 \omega_{BW}}{Z_0 \omega_0^2 J_\mathrm{r}^2} \tag{3.1.3c}$$

An intuitive look at equation 3.1.3c reveals that if L_p is to remain constant with a change in centre frequency, ω_0, then the absolute bandwidth, ω_{BW}, has to change proportionately with ω_0 in order to preserve the validity of the equation. If a constant absolute bandwidth is to be maintained, then J_r needs to be tunable as well. Such an implementation becomes complicated as it shall be shown in the next section that multiple elements are dependent on the implementation of J_r. Instead, J_r will be kept constant and ω_{BW} will be allowed

to change as the resonator is tuned.

3.2 Conversion of ideal inverters to lumped element approximates

The inverters used in the circuit models up to this point have been assumed to be ideal and frequency independent. Such inverters do not exist in practice, but can be approximated with lumped elements over a limited frequency range. Recall that the admittance inverters can be implemented with pi-networks shown in figure 3.3. The frequency independent susceptances can be approximated with lumped elements at an operating frequency of ω_π as follows:

$$|B| = \omega_\pi C \tag{3.2.1}$$

and

$$|B| = \frac{1}{\omega_\pi L}. \tag{3.2.2}$$

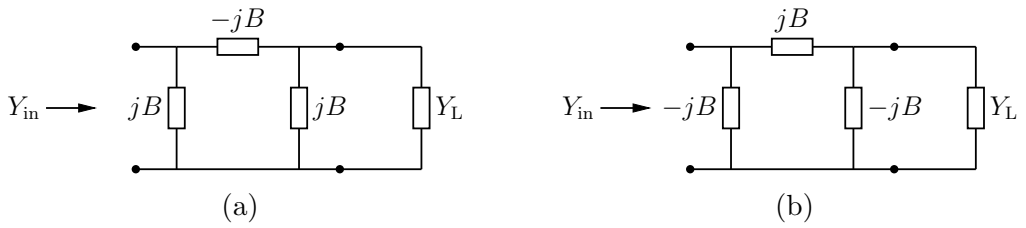

Figure 3.3: Pi-model representations of admittance inverter circuit. (a) Configuration for a $+90°$ phase shift. (b) Configuration for a $-90°$ phase shift.

Table 3.2 shows lumped element inverter approximations with their frequency response based on a normalised implementation at an operating frequency of $\omega_\pi = 1$rads/s with $Y_\mathrm{L} = 1$ and $C = L = 1$. The bandwidth for which $S_{11} \leq -20$dB gives an indication of the limited frequency range for which the approximations are valid.

Table 3.2: Comparison of inverter implementations

	Inverter circuit model	Frequency response curve
I	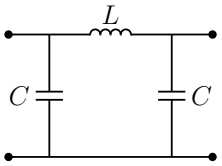	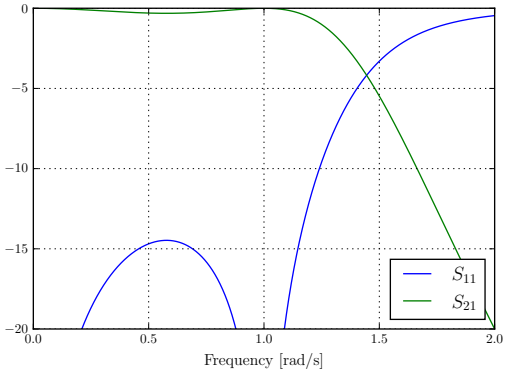
II	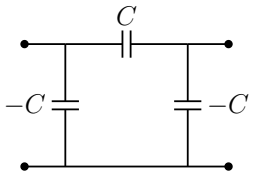	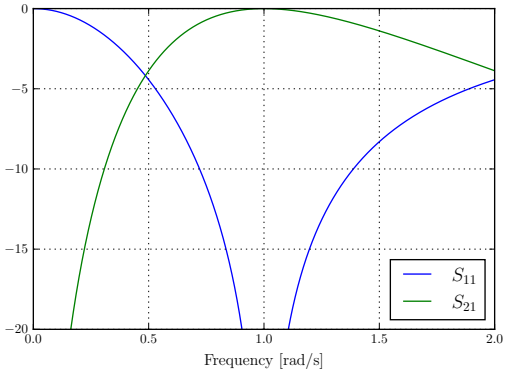
III	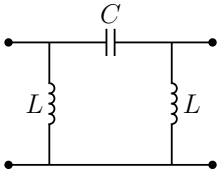	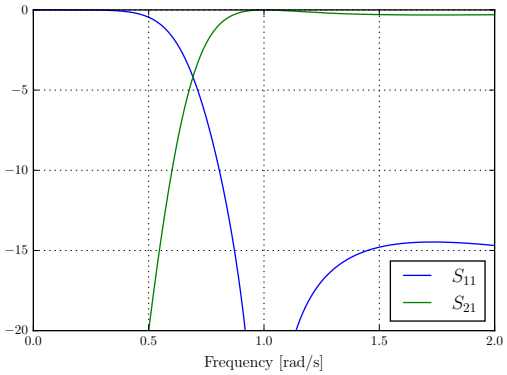
IV	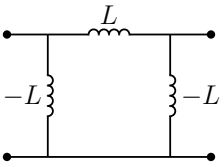	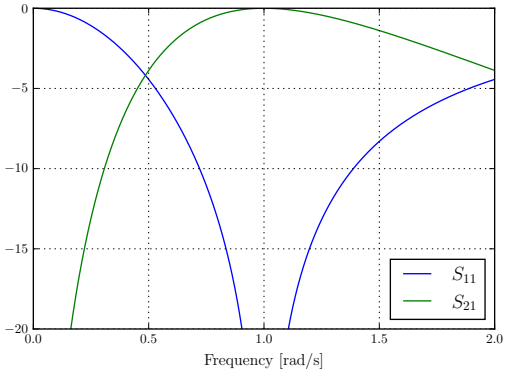

Based on the data presented in table 3.2, topology I exhibits a lowpass response overall whereas topology III exhibits a highpass response overall. Topologies II and IV exhibit a bandpass response overall centred around the operating frequency.

Recall that the EW system operates between 20-500MHz and the notch needs to be tuned between 400-490MHz. If the operating frequency for all of the inverters is chosen as 445MHz which is the centre frequency of the tuning range, then it is best to implement J_{12} and J_{23} with topology I to allow signals below the operating frequency to pass through the network. For J_{r} it is best to implement topology II as the negative capacitor values can be absorbed into the circuit and the parallel LC tank resonators need only to operate between the tuning range of 400-490MHz. The revised circuit model with lumped element inverters is shown in figure 3.4.

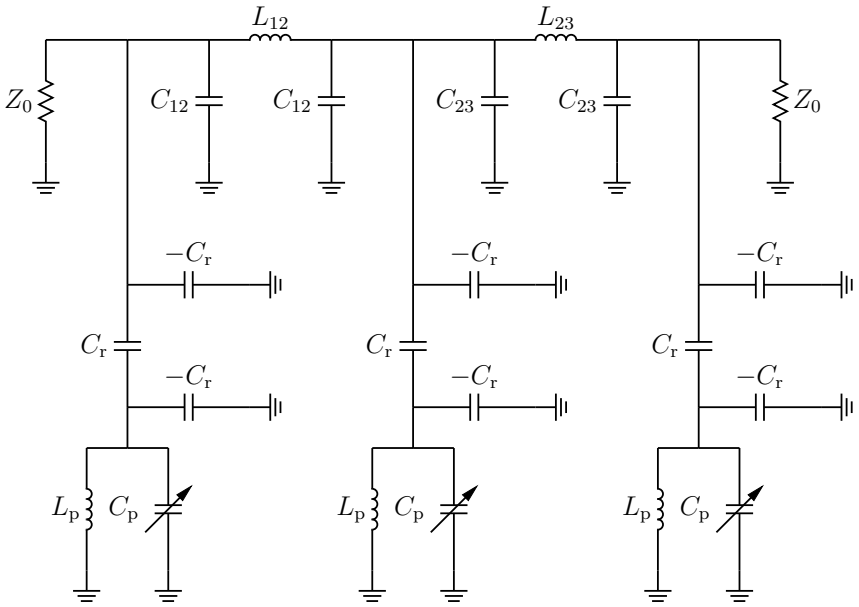

Figure 3.4: Revised notch filter circuit with lumped element inverters

The inverter element values are as follows:

$$C_{12} = \frac{J_{12}}{\omega_\pi} = 8.62985\mathrm{pF} = C_{23} \tag{3.2.3}$$

$$L_{12} = \frac{1}{\omega_\pi J_{12}} = 14.82235\mathrm{nH} = L_{23} \tag{3.2.4}$$

$$C_{\mathrm{r}} = \frac{J_{\mathrm{r}}}{\omega_\pi} \tag{3.2.5}$$

Figure 3.5 shows the final notch filter circuit model where the negative elements shown in figure 3.4 have been absorbed into the circuit. The updated element values are as follows:

$$C'_{12} = C_{12} - C_{\mathrm{r}} = C'_{23} \tag{3.2.6}$$

$$C''_{12} = C_{12} - \frac{C_{\mathrm{r}}}{2} = C''_{23} \tag{3.2.7}$$

$$C'_{\mathrm{p}} = C_{\mathrm{p}} - C_{\mathrm{r}} \tag{3.2.8}$$

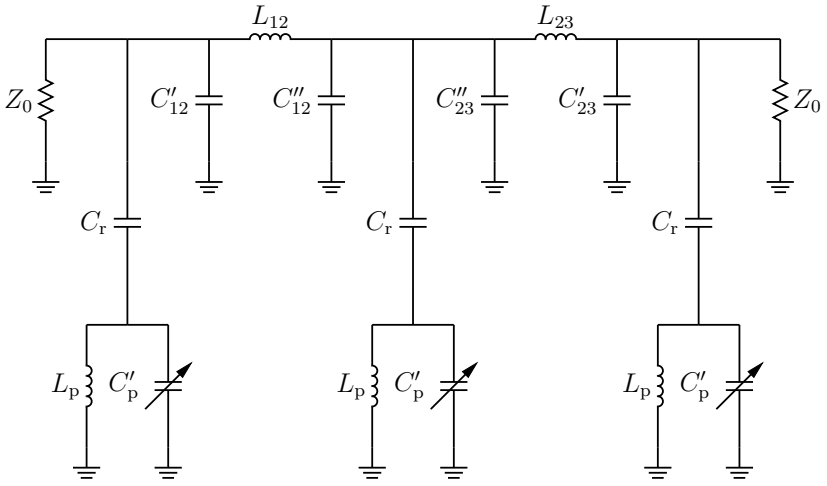

Figure 3.5: Final notch filter circuit with lumped element inverters

3.3 Non-ideal lumped elements and semiconductors

The parasitics and losses in practical lumped element and semiconductor components are often assumed to be negligible for very low frequency applications. For RF applications, such assumptions cannot be made as the parasitics and losses in components become increasingly noticeable as frequency increases. A good understanding of the modelling of non-ideal behaviour is important for component selection as it can make the difference between selecting a "good" or a "bad" component based on the data that is made available by the manufacturers.

3.3.1 Inductors

Out of all the passive lumped elements, practical inductors deviate the most from ideal behaviour at RF. Figure 3.6a shows a distributed model of a typical inductor with an equivalent circuit shown in figure 3.6b [17,24]. The loss in the inductor is modelled by the series resistor, R_{s}, which directly impacts the Q-factor of the inductor. The distributed capacitance between the individual coils is modelled by the parallel capacitor, C_{d}, which limits the frequency range over which the inductor can be used.

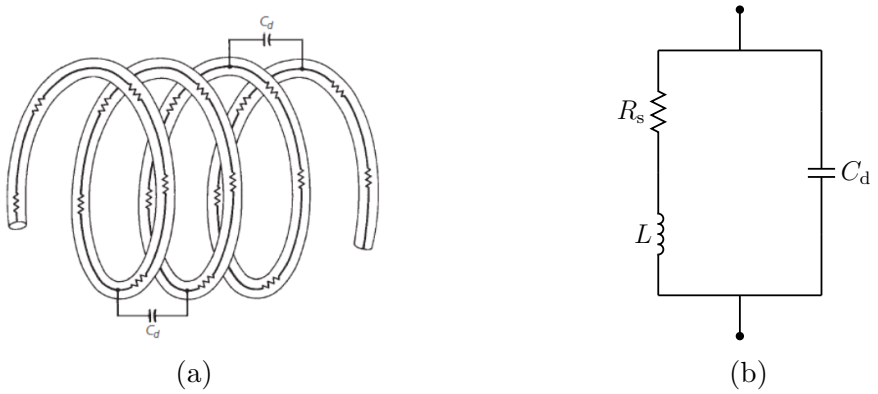

(a) (b)

Figure 3.6: (a) Distributed inductor model. (b) Equivalent circuit model.

The impedance, $|Z_L|$, of an ideal inductor increases linearly with frequency, but for a non-ideal inductor this linearity is only observed at low frequencies. As frequency increases, the effects of the distributed capacitance become more noticeable and this causes a non-linear surge in impedance to a finite peak value shown in figure 3.7 [9, 17]. The peak corresponds to the condition where the inductor becomes parallel resonant. The frequency at which the inductor is parallel resonant with the distributed capacitance is termed the *self-resonant frequency* (SRF) [24,25]. The SRF along with a typical Q-factor is often provided in the datasheet of a particular inductor. The series resistor and parallel

capacitor for the model in figure 3.6b can be determined as follows:

$$R_{\mathrm{s}} = \frac{\omega L}{Q} = \frac{|X_L|}{Q} \tag{3.3.1}$$

and

$$C_{\mathrm{d}} = \frac{1}{(2\pi f_{\mathrm{SRF}})^2 L}. \tag{3.3.2}$$

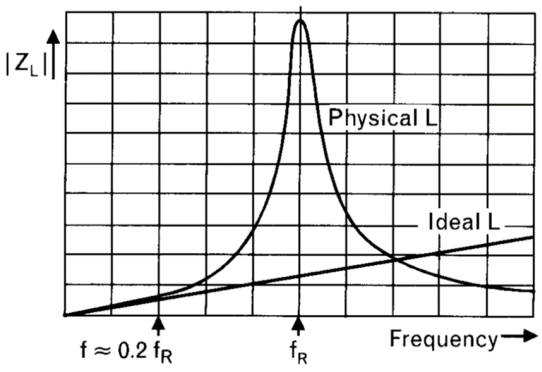

Figure 3.7: Inductor impedance versus frequency

Due to the non-linear behaviour of $|Z_L|$ at high frequencies, the effective inductance of the inductor at these frequencies is higher than its nominal value [9, 24]. The nominal inductance value that is specified in the datasheet of a particular inductor is usually measured at low frequencies. The effective inductance value for high frequencies can be approximated as

$$L_{\mathrm{eff}} \approx \frac{L}{1-(f/f_{SRF})^2}. \tag{3.3.3}$$

As a rule of thumb, the model in figure 3.6b can only give reasonable predictions for frequencies up to $f_{SRF}/5$ [9,24]. It assumes that R_{s} remains constant and does not account for the skin effect at high frequencies. The skin effect occurs when the current density around the centre of the cross-section of the inductor wire decreases with an increase in frequency resulting in a greater current density at the edge of the cross-section shown in figure 3.8 [17]. This causes R_{s} to increase with frequency which will result in a lower Q-factor than what is predicted by the model in figure 3.6b.

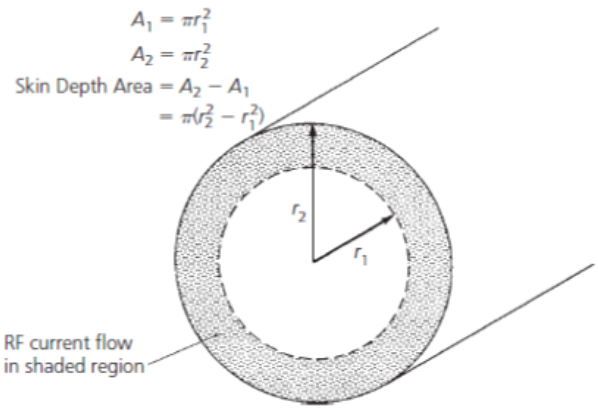

Figure 3.8: Illustration of the skin effect

3.3.2 Capacitors

The capacitance of a multilayer parallel plate capacitor, as shown figure 3.9, can be determined as follows:

$$C = \frac{\epsilon_0 \epsilon_r A(n-1)}{d}, \tag{3.3.4}$$

where ϵ_0 is the permittivity of free space, ϵ_r is the relative dielectric constant, A is the surface area of the electrodes, n is the number of electrodes and d is the spacing between the electrodes [9, 25]. The effects of fringing fields are assumed to be negligible.

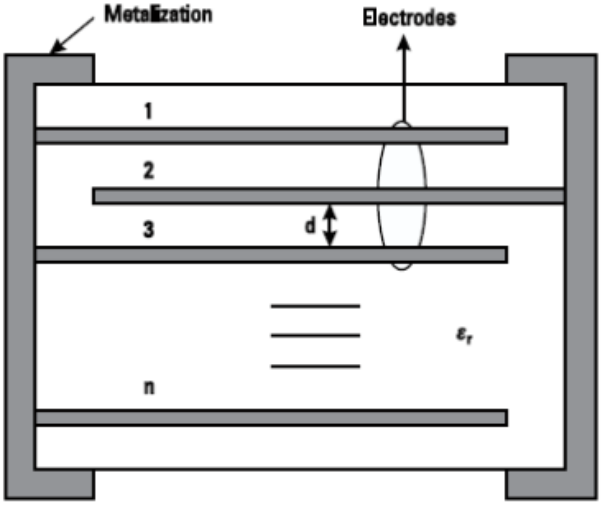

Figure 3.9: Multilayer parallel plate capacitor

Figure 3.10a shows an equivalent circuit model of a typical capacitor [17]. The loss in the capacitor is modelled by the series resistor, R_s. The parasitic inductance of the conducting surface is modelled by L_s. The dc leakage current through the capacitor is modelled by R_p, known as the insulation resistance, which is often in the order of

gigaohms. Figure 3.10b shows a simplified circuit model which is adequate for frequencies where the effect of the parasitic inductance is negligible.

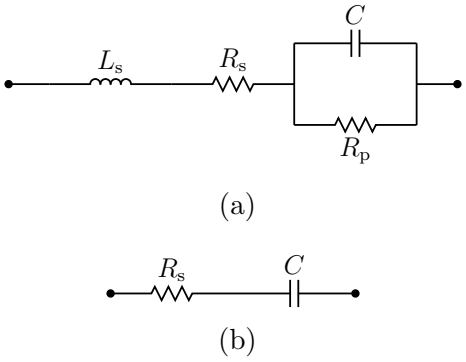

Figure 3.10: Equivalent circuit models for a capacitor. (a) Complete model. (b) Simplified model

Just like an inductor, a capacitor also has a limited frequency range over which it can be used due to a SRF corresponding to the condition when the capacitor is series resonant with the parasitic inductance [25]. The SRF along with a typical Q-factor is often provided in the datasheet of a particular capacitor. The series resistor and parasitic inductor for the model in figure 3.10a can be determined as follows:

$$R_s = \frac{1}{\omega C Q} = \frac{|X_C|}{Q} \tag{3.3.5}$$

and

$$L_s = \frac{1}{(2\pi f_{SRF})^2 C}. \tag{3.3.6}$$

The dissipation factor, which is often expressed as a percentage, is an indication of the approximate power lost in a capacitor as heat and is defined as

$$\mathrm{DF} = \frac{R_s}{|X_C|} = \frac{1}{Q}, \tag{3.3.7}$$

which is a useful parameter to lookout for if the Q-factor is not provided by the manufacturer of a particular capacitor [17].

At high frequencies, the impedance of a capacitor starts to deviate from its ideal value due to the parasitic inductance [9, 25]. This deviation results in a higher effective capaci-

tance value which can be approximated as

$$C_{\text{eff}} \approx \frac{C}{1-(f/f_{SRF})^2}. \tag{3.3.8}$$

Temperature stability is a final factor to consider. The temperature coefficient (TC) of a capacitor determines the rate of change in capacitance due to temperature. Most small-value capacitors that are used for RF applications are temperature stable and have a low a TC typically less than $\pm 50\text{ppm}/^oC$ [25].

3.3.3 Varactor diodes

Varactor diodes are P-N junction diodes with the property that their capacitance can be varied as a function of a reverse bias voltage, V_{r}, applied to them shown in figure 3.11 [26, 27]. They are best suited for applications where continuous tuning is implemented. There are two types of varactors, abrupt and hyperabrupt, which have different doping structures. The junction capacitance of a varactor can be determined as follows:

$$C_{\text{j}}(V_{\text{r}}) = \frac{C_{\text{j0}}}{(V_{\text{r}}/\Phi + 1)^{\gamma}}, \tag{3.3.9}$$

where C_{j0} is the capacitance of the varactor for a 0V bias, Φ is the built-in potential of the varactor and γ is a constant based on the doping structure [27]. For an abrupt varactor, γ is approximately in the order of 0.47 to 0.5, whereas for a hyperabrupt varactor, γ is approximately in the order of 0.75 to 1.5. The $\log(C_{\text{j}})$ vs. $\log(V_{\text{r}} + \Phi)$ capacitance-voltage relationships for abrupt and hyperabrupt varactors are shown in figures 3.12a and 3.12b respectively [27].

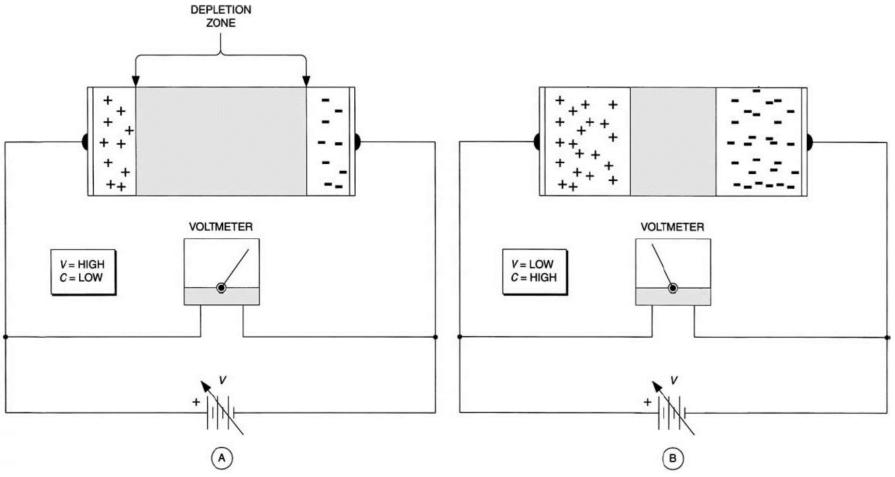

Figure 3.11: Working of a varactor diode

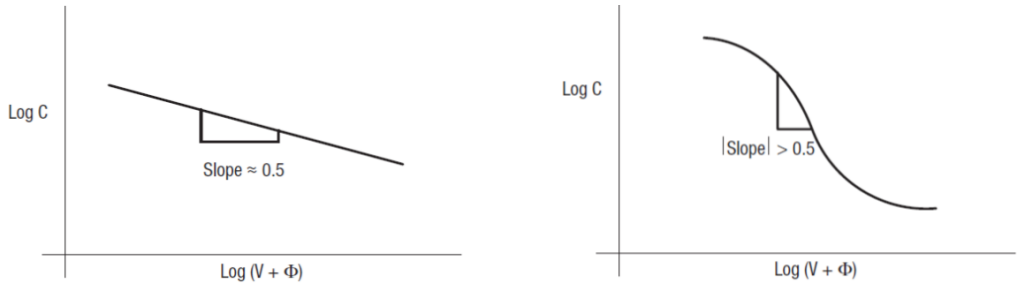

(a) (b)

Figure 3.12: Capacitance-voltage relationship for: (a) abrupt and (b) hyperabrupt varactors.

Based on the capacitance-voltage relationships shown in figures 3.12a and 3.12b, abrupt varactors are better suited for applications where fine tuning is required with a gradual change in capacitance, whereas hyperabrupt varactors are better suited for wide tuning ranges. An equivalent circuit model for a lossy varactor is shown in figure 3.13. The loss in the varactor is modelled by the series resistance, $R_{\mathrm{s}}(V_{\mathrm{r}})$, which decreases as the bias voltage increases. The parasitic inductance and capacitance of the package where the diode comes in is modelled by L_{s} and C_{p} respectively. The values of the elements in the model are usually provided in the datasheet for a specific varactor.

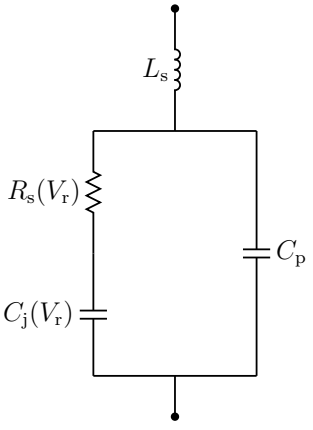

Figure 3.13: Equivalent circuit model for a varactor diode

The Q-factor of the varactor is

$$Q = \frac{1}{\omega C_{\mathrm{j}}(V_{\mathrm{r}}) R_{\mathrm{s}}(V_{\mathrm{r}})}. \tag{3.3.10}$$

Most SPICE models assume that $R_{\mathrm{s}}(V_{\mathrm{r}})$ is constant and base it on a maximum value. In that case, the Q-factor can be approximated as

$$Q \approx \frac{1}{\omega C_{\mathrm{j}}(V_{\mathrm{r}}) R_{\mathrm{s(max)}}}. \tag{3.3.11}$$

3.3.4 Digitally tunable capacitors

A digitally tunable capacitor (DTC) is an integrated circuit (IC) that consists of a network of small capacitors that form a parallel capacitor bank shown in figure 3.14a [28]. Each capacitor has a designated MOSFET switch that controls whether or not the capacitor should be switched into the bank at a given time. The capacitance values of the DTC are discrete and each correspond to a digital state. A DTC is thus best suited for applications where discrete tuning is implemented.

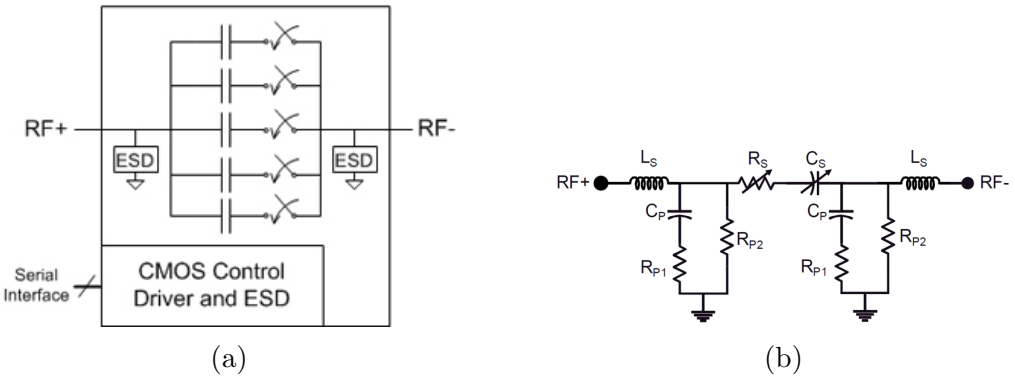

Figure 3.14: (a) Block diagram of DTC. (b) Equivalent circuit model of DTC

Figure 3.14b shows an equivalent circuit model of the DTC [28]. The loss in the bias networks is modelled by R_{p1} and R_{p2}. The loss within the tuning core is modelled by R_{s}. The parasitic inductance and capacitance of the package is modelled by L_{s}, C_{p1} and C_{p2}. Apart from L_{s} and R_{p1}, the values of the components in the model are different for each state which means that the model has to be updated regularly when implemented in a simulations. The Q-factor of the tuning core is

$$Q = \frac{1}{\omega C_{\mathrm{s}} R_{\mathrm{s}}}. \tag{3.3.12}$$

The typical Q-factors for the different DTCs available are significantly lower than those of varactor diodes. The DTC requires a digital control system to change its states, whereas varactor diodes require large bias voltages for tuning which can easily be done with laboratory DC supplies. In terms of quality and convenience, varactor diodes are a better choice to implement.

3.4 Filter implementation with real components

The circuitry of the filter is implemented on a low-loss printed circuit board (PCB) with surface-mount technology (SMT) [29]. Surface-mount components have less parasitic effects, when compared to leaded components, making them more suitable to use at RF. All practical components exhibit some form of tolerance which results in a component's nominal value deviating from its ideal value. To minimise this effect, a single element is often realised with two or more components in parallel. Excerpts from the datasheets of the components used can be found in appendix A.

In chapter 2 it was shown that the Q-factors of the resonators in the filter dictate its stopband performance greatly. The objective here is to select components in such a way that the overall Q-factor of each LC tank circuit is maximised. The highest-Q inductors suitable to be implemented are mini spring air core inductors from Coilcraft. A single 4nH inductive element is realised from two 8nH inductors in parallel each having a Q-factor of approximately 185 at 445MHz. The SRF of the inductors is in the order of 5GHz which means that the effective inductance should be close to its nominal value. The tuning curve for the capacitive element in the tank circuit corresponding to this inductor selection is shown in figure 3.15.

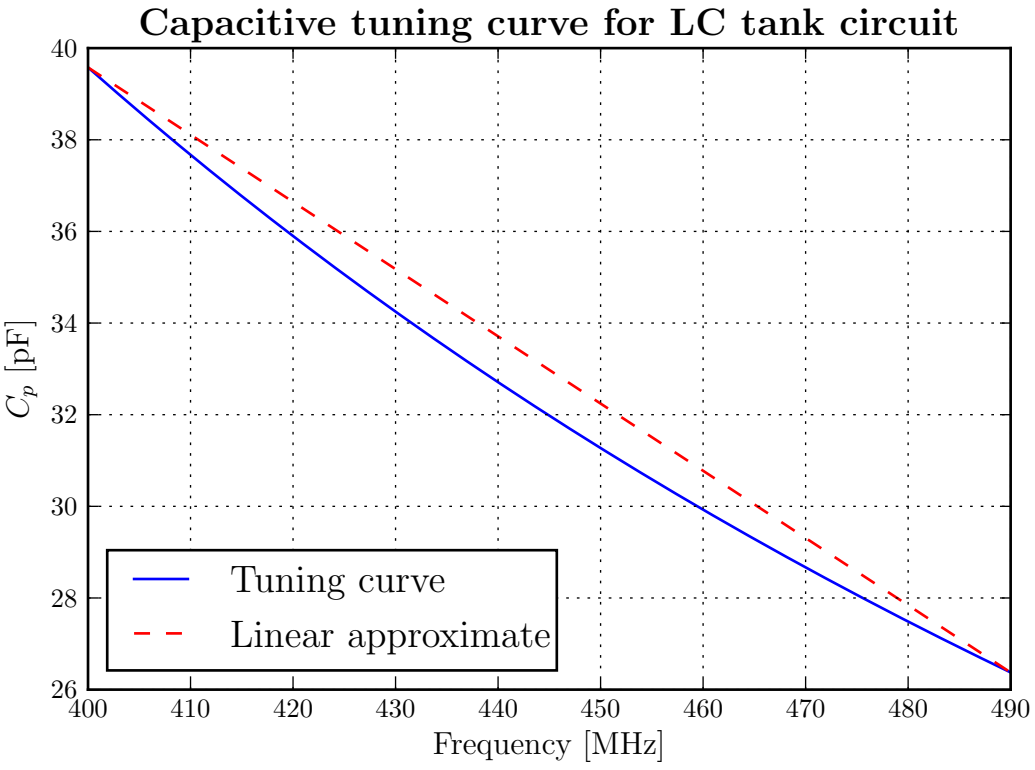

Figure 3.15: Tuning curve for LC tank circuit

From the plot shown in figure 3.15, the approximate upper and lower limits of the capacitive element in the resonator is 40pF and 26pF respectively. The tuning curve fits the profile of an abrupt varactor diode. Two configurations to implement varactor diodes are shown in figure 3.16. A back-to-back configuration offers more linearity, but this halves the overall capacitance. Diodes implemented with a back-to-back configuration would require more components in parallel compared to an implementation with a single diode configuration. To keep the number of components required to a minimum, a single diode configuration is implemented. The SMV1413 abrupt varactor diode from Skyworks offers the best price for performance. A single diode configuration comprising of six varactors (in parallel) with a series 4.7nF DC block capacitor is placed in parallel with two 6.2pF capacitors to form a tunable capacitive element. A single voltage bias is implemented to tune all three resonators. The approximate Q-factor of the varactors is 250 at 445MHz which is higher than that of the inductors. It can be concluded that the inductors will limit the performance of the resonator.

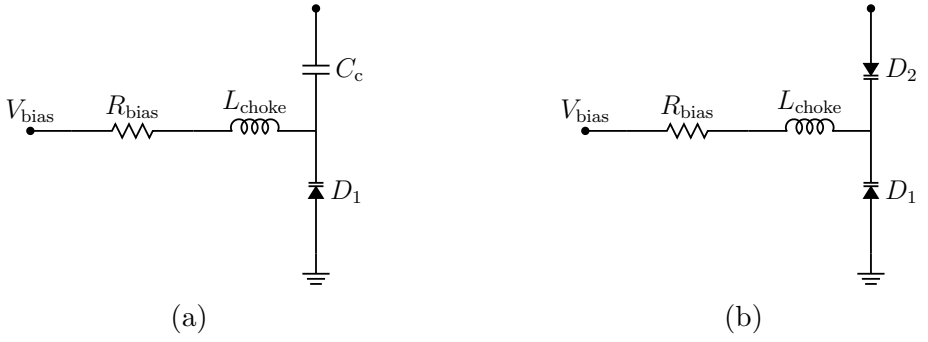

Figure 3.16: Biasing networks for diode circuits: (a) Single diode configuration and (b) back-to-back diode configuration.

The capacitor, C_{r}, for the resonator inverters is determined from design equations 2.8.16 and 3.2.5 as 1.9pF. This capacitor is realised with a 1.8pF capacitor with its negative values in the inverter easily absorbed into the rest of the circuit. The remaining capacitive elements in the J_{12} and J_{23} inverters are realised with two 3.6pF capacitors in parallel which is a rough approxmimation of the desired value. All capacitors used are high-Q RF capacitors from KEMET and will have the least losses out of all the components. The inductive elements in the J_{12} and J_{23} inverters are realised with two 28nH air core inductors in parallel. A complete circuit model of the filter is presented in 3.17 which includes modelling of losses for simulation purposes. A graphical impression of the filter implementation is shown in figure 3.18.

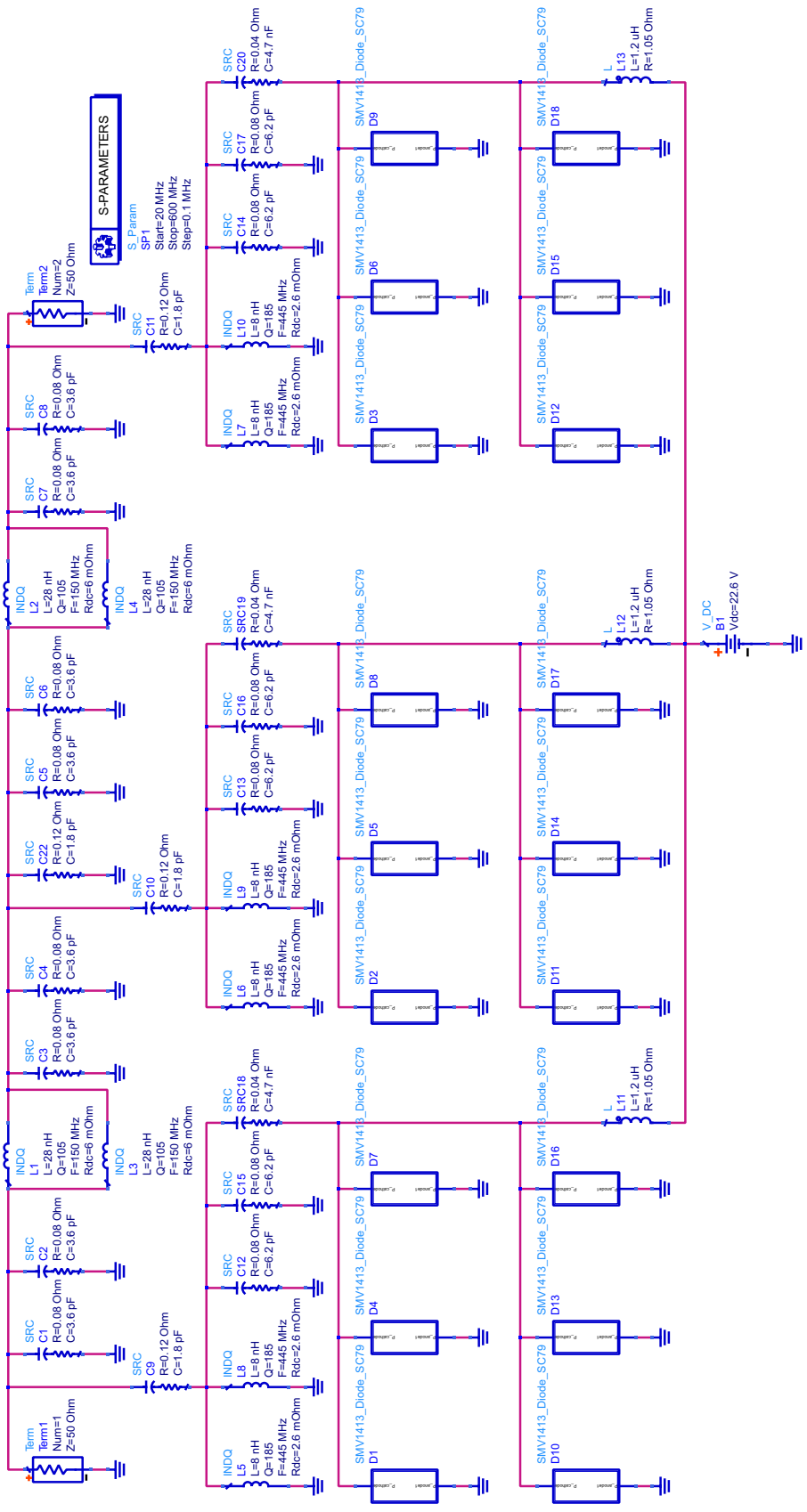

Figure 3.17: Filter implementation circuit schematic

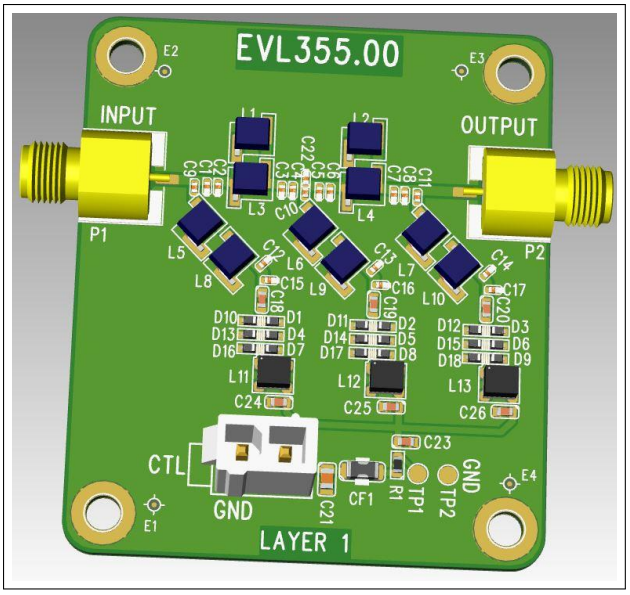

Figure 3.18: Graphical impression of filter implementation

A simulation of the filter was performed in ADS with the results shown in figure 3.19. The null rejection is 10dB at 400MHz and 24dB at 490MHz. The change in null rejection is primarily due to the Q-factors of the inductors changing substantially with frequency. The maximum passband insertion loss is approximately 1.2dB. Two to three filters could be placed in cascade to improve the null rejection without impacting the insertion loss too seriously.

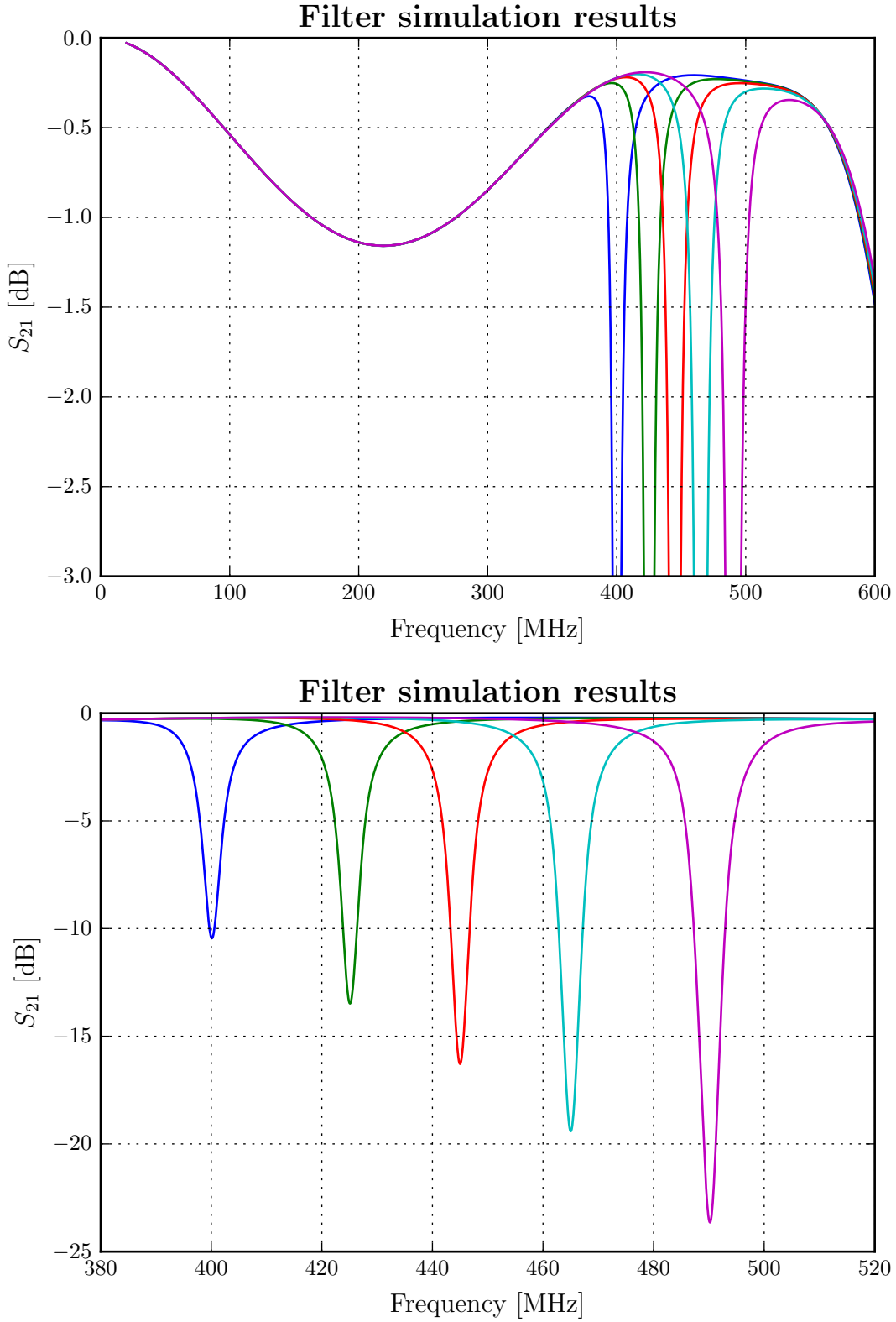

Figure 3.19: Filter simulation results

Chapter 4

Non-linear distortion

Throughout the synthesis and implementation phases presented in chapters 2 and 3 respectively, the filter has been assumed to be a linear system. A linear system is a system for which the principle of superposition holds true [30]. For example, if two separate excitations x_1 and x_2 are applied to a system producing separate responses y_1 and y_2 respectively, then the combined excitation of $\alpha x_1 + \beta x_2$ must produce a combined response of $\alpha y_1 + \beta y_2$. In practice, all electronic systems exhibit some form of non-linear behaviour [10]. This chapter will discuss the impact that non-linear behaviour can have on the performance of the filter from a systems approach. The concept of dynamic range, which was briefly introduced in chapter 1, is revisited in order to characterise the performance of the filter.

4.1 Taylor series analysis of non-linear behaviour

The filter can be considered as a weakly non-linear system driven by a small-signal excitation shown in figure 4.1, where v_i and v_o are the small-signal input and output voltages respectively [11]. The non-linear output voltage can be approximated (up to a third-order) as a truncated Taylor series in terms of the input voltage as follows:

$$v_0 \approx k_0 + k_1 v_i + k_2 v_i^2 + k_3 v_i^3, \tag{4.1.1}$$

where

$$k_n = \left. \frac{d^n v_0}{dv_i^n} \right|_{v_i=0}. \tag{4.1.2}$$

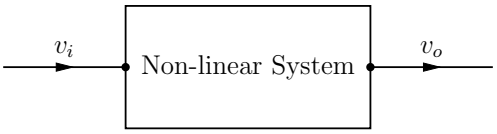

Figure 4.1: Block representation of a non-linear system

Consider a two-tone excitation described by

$$v_i = V_1 \cos(\omega_1 t) + V_2 \cos(\omega_2 t), \tag{4.1.3}$$

where ω_1 and ω_2 are the fundamental frequencies of the two excitations.

The output voltage can be determined by substituting equation 4.1.3 into equation 4.1.1 to obtain

$$\begin{aligned} v_0 \approx\ & k_0 + k_1(V_1 \cos(\omega_1 t) + V_2 \cos(\omega_2 t)) \\ & + k_2(V_1 \cos(\omega_1 t) + V_2 \cos(\omega_2 t))^2 \\ & + k_3(V_1 \cos(\omega_1 t) + V_2 \cos(\omega_2 t))^3 \qquad (4.1.4a) \\ \approx\ & k_0 + k_1(V_1 \cos(\omega_1 t) + V_2 \cos(\omega_2 t)) \\ & + \frac{1}{2}k_2\{V_1^2 + V_2^2 + V_1^2 \cos(2\omega_1 t) + V_2^2 \cos(2\omega_2 t) \\ & + 2V_1V_2[\cos((\omega_1 + \omega_2)t) + \cos((\omega_1 - \omega_2)t)]\} \\ & + \frac{1}{4}k_3\{V_1^3 \cos(3\omega_1 t) + V_2^3 \cos(3\omega_2 t) \\ & + 3V_1^2V_2[\cos((2\omega_1 + \omega_2)t) + \cos((2\omega_1 - \omega_2)t)] \\ & + 3V_1V_2^2[\cos((\omega_1 + 2\omega_2)t) + \cos((\omega_1 - 2\omega_2)t)] \\ & + 3(V_1^3 + V_1V_2^2)\cos(\omega_1 t) + 3(V_2^3 + V_1^2V_2)\cos(\omega_2 t)\}, \qquad (4.1.4b) \end{aligned}$$

which contains additional frequency components in the form of harmonics and mixing products of the fundamental frequencies [30]. These additional frequency components at the output of the system are collectively referred to as *intermodulation products* (IM products) and can be described by

$$\omega_{mn} = m\omega_1 + n\omega_2, \tag{4.1.5}$$

where m and n are integer values. The order of a specific IM product is defined as $|m| + |n|$ [16, 30]. Figure 4.2 shows a typical spectrum of the output voltage of a non-linear system excited by a two-tone source. The generation of IM products at the output of a system is termed *intermodulation distortion* [10, 11].

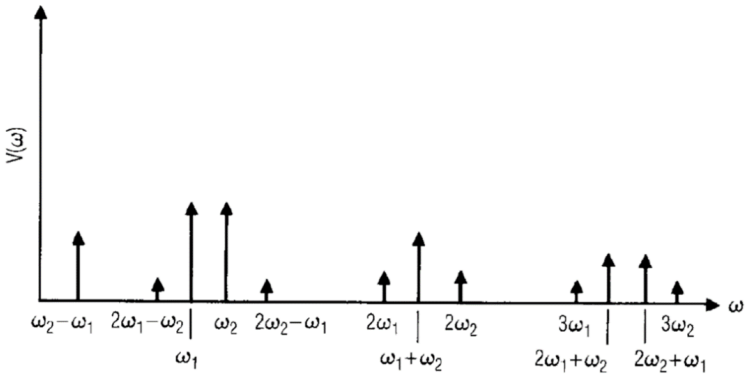

Figure 4.2: Typical spectrum of the output voltage of a non-linear system excited by a two-tone source

4.2 Dynamic range

In chapter 1, the linear dynamic range (LDR) was defined as the range between the maximum allowed input signal power and the minimum detectable signal (MDS) power that the jammer receiver can handle without its amplifiers going into saturation. In the particular case of the filter, which is a passive system, the LDR can be defined as the range between the maximum input signal power that the filter can physically handle and the noise floor.

When harmonics and mixing products are generated at the output of a non-linear system, they are often referred to as *spurious responses* [30]. Spurious responses are undesirable as they can occur at frequencies where other signals exist causing interference. The signal power of the spurious responses is directly proportional to the signal power of the fundamental tones at the output. The *spurious free dynamic range* (SFDR) is defined as the range between the maxium output signal power and the noise floor for which there are no spurious responses visible at the output [9, 16]. In the particular case of the filter, the signals responsible for producing spurious responses are mainly strong signals from friendly radio devices in close proximity of the filter. The filter is only in use when these devices utilise the 400-490MHz (UHF PMR) communications band which lies in the upper half of the filter's passband. The spurious responses of particular interest are the third-order IM products of $2\omega_1 - \omega_2$ and $2\omega_2 - \omega_1$ as they are guaranteed to fall within the filter's passband whereas other spurious responses will fall outside of the filter's passband. Figure 4.3 illustrates the relationship between the signal power of the fundamental tones and the third-order IM products. The output signal power of the third-order IM products increases by 3dB for every 1dB increase in output signal power of the fundamental tones [9]. The *third-order intercept point*, IP_3, is a theoretical intercept point where the output signal power of the the fundamental tones and the third-order IM

products are equal [10].

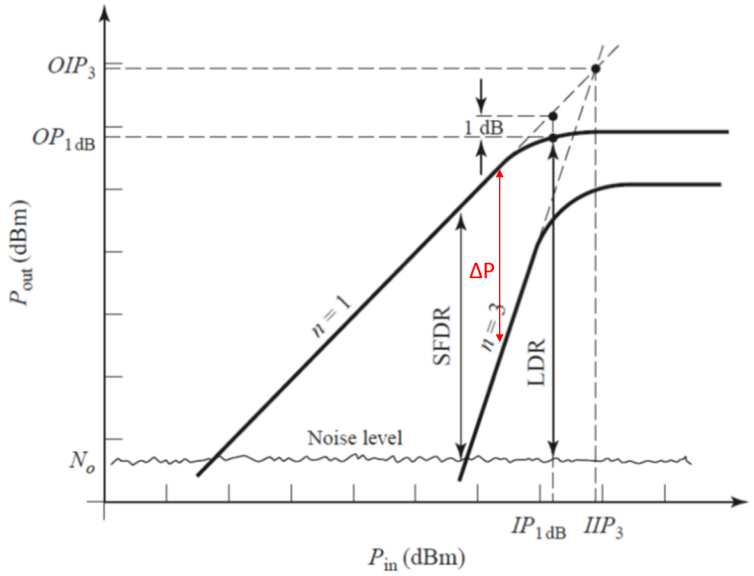

Figure 4.3: Graphical representation of the LDR and SFDR of a system

The LDR and SFDR can be derived by graphical methods from figure 4.3 to yield:

$$\text{LDR (dB)} = OP_{1\text{dB}} - N_o \tag{4.2.1}$$

and

$$\text{SFDR (dB)} = \frac{2}{3}(OIP_3 - N_o), \tag{4.2.2}$$

where $OP_{1\text{dB}}$ is the maximum output power of the fundamental tones, OIP_3 is the output power of the third-order intercept point and N_o is the noise floor [10, 16].

In practice, the third-order intercept point cannot be measured as it lies at a power level that the system cannot handle. Instead, it is extrapolated from measured data such as that presented in figure 4.4. The third-order intercept point based on measured data can be derived by graphical methods from figure 4.3 to yield:

$$OIP_3 = P_{\omega_1} + \frac{\Delta P}{2}, \tag{4.2.3}$$

where P_{ω_1} is the measured power of the fundamental tones and ΔP is the power difference between the fundamental tones and the third-order IM products [10].

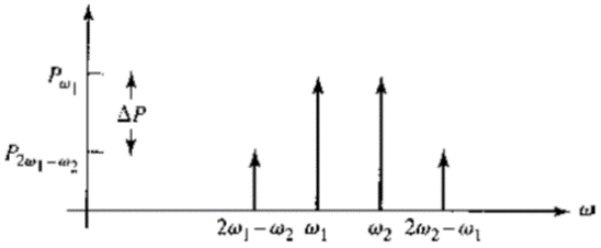

Figure 4.4: Typical spectrum of measured fundamental tones and third-order IM products

4.3 Simulation results

A harmonic balance simulation was performed in ADS with a two-tone excitation. The frequencies of the fundamental tones were chosen as $f_1 = 445$MHz and $f_2 = 445.01$MHz corresponding to the centre frequency of the UHF PMR communications band which is also the centre frequency of the tuning range. The notch of filter was tuned down to 400MHz so not to attenuate the output signal power of the excitations and also to ensure that the diodes in the filter were biased with a low voltage (4V) for a worse case scenario in terms of their non-linear behaviour. The simulation results are presented in figure 4.5.

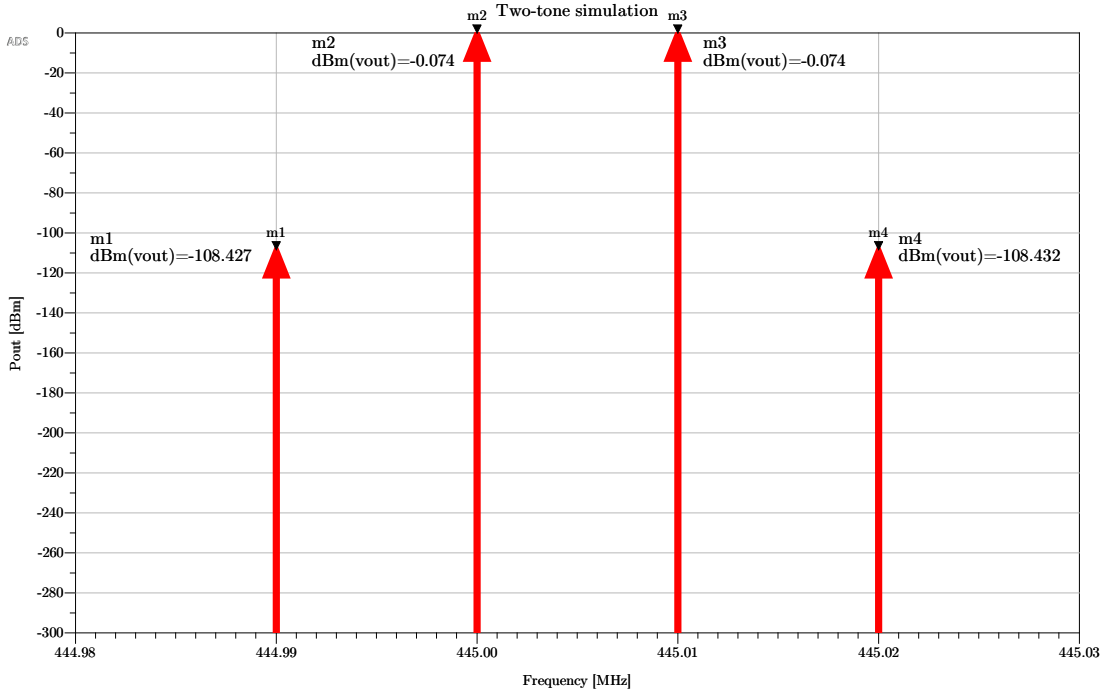

Figure 4.5: Spectrum for two-tone simulation results

From the results in figure 4.5 it is clear that spurious responses are present in the output. If a typical noise floor of -100dBm is assumed, then the spurious responses lie just below the noise floor. With a ΔP of approximately 108dBm between the signal power of the fundamental frequencies and the IM products, the third-order intercept point is determined as 54dBm. Based on this point and the assumption of the noise floor, the SFDR is determined as 102dB. The SPICE model for the diodes used models the series resistor, R_{s}, as a constant based on a maximum value. This is not true for a practical diode and more non-linear behaviour is expected when practical measurements are taken.

Chapter 5

Practical measurements

This chapter discusses the practical measurements obtained from the filter circuit that was assembled. Laboratory DC supplies were used to bias the varactor diodes to control the tuning. The s-parameters of the filter were measured on a vector network analyzer (VNA) to evaluate the passband and stopband characteristics as well as the tuning range. Where possible, diagnostics and modifications have been made to improve the filter's performance. The chapter concludes by presenting the results of a two-tone test measured on a spectrum analyser which characterises the filter's non-linear behaviour.

5.1 S-parameter measurements

The initial S-parameter measurements are shown in figure 5.1. The tuning range is 400-423MHz and the null rejection ranges between 5.4dB and 6dB. These results are poor in comparison to what was predicted in the simulation (with losses accounted for). Reasons for these results include mutual coupling between parallel inductors which increases the effective inductance and decreases the Q-factor of the inductors. The nulls do not form perfectly at the same frequency due to the effect of the different tolerances in the components used in the resonators. These diagnostics were confirmed by importing the results into ADS and adjusting the circuit model to match the results shown in figure 5.2. Figure 5.3 shows an equivalent circuit model for coupled parallel inductors. The additional inductance, L_{M}, was determined experimentally in ADS as 2nH for the inductors used in the resonators.

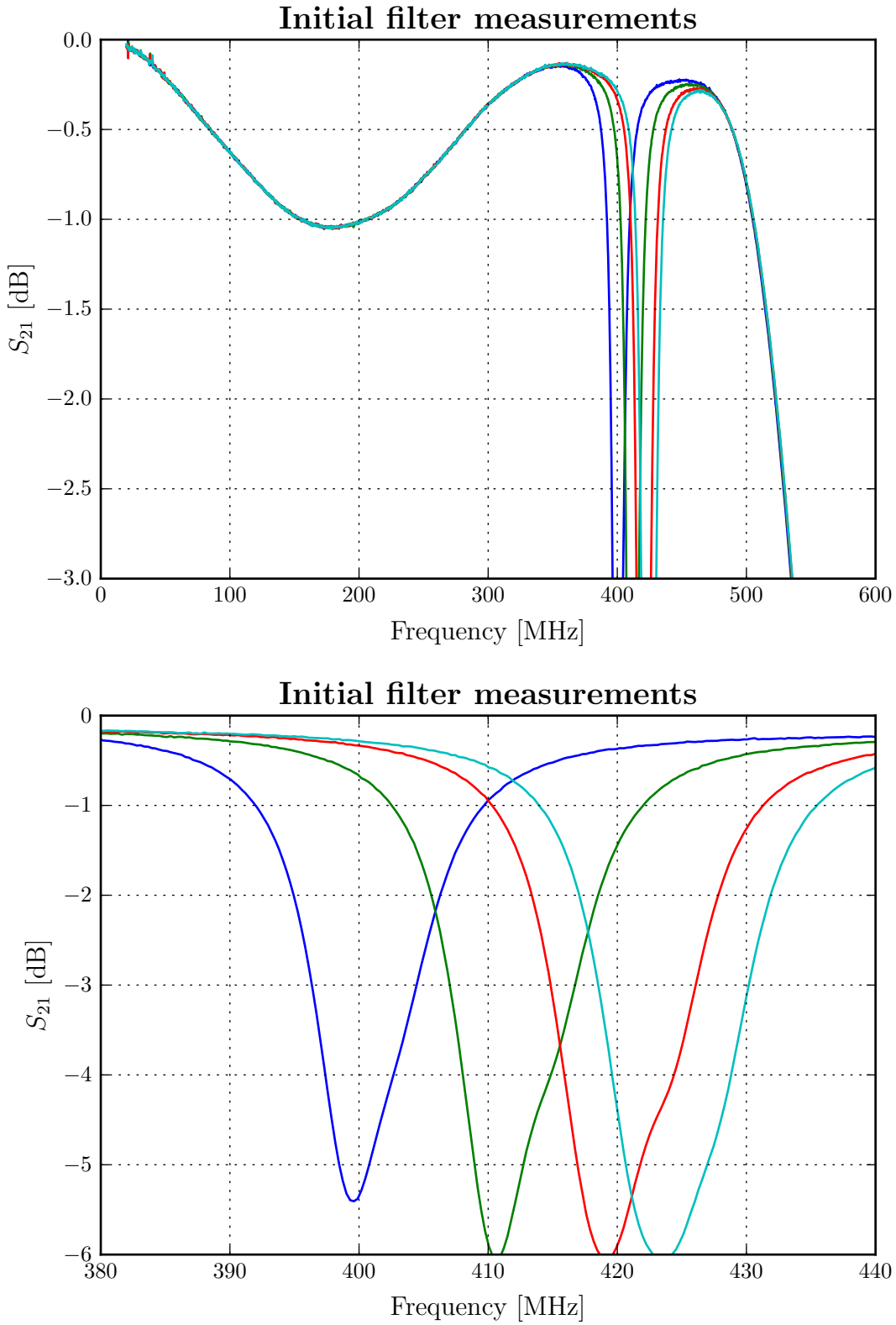

Figure 5.1: Initial filter measurements

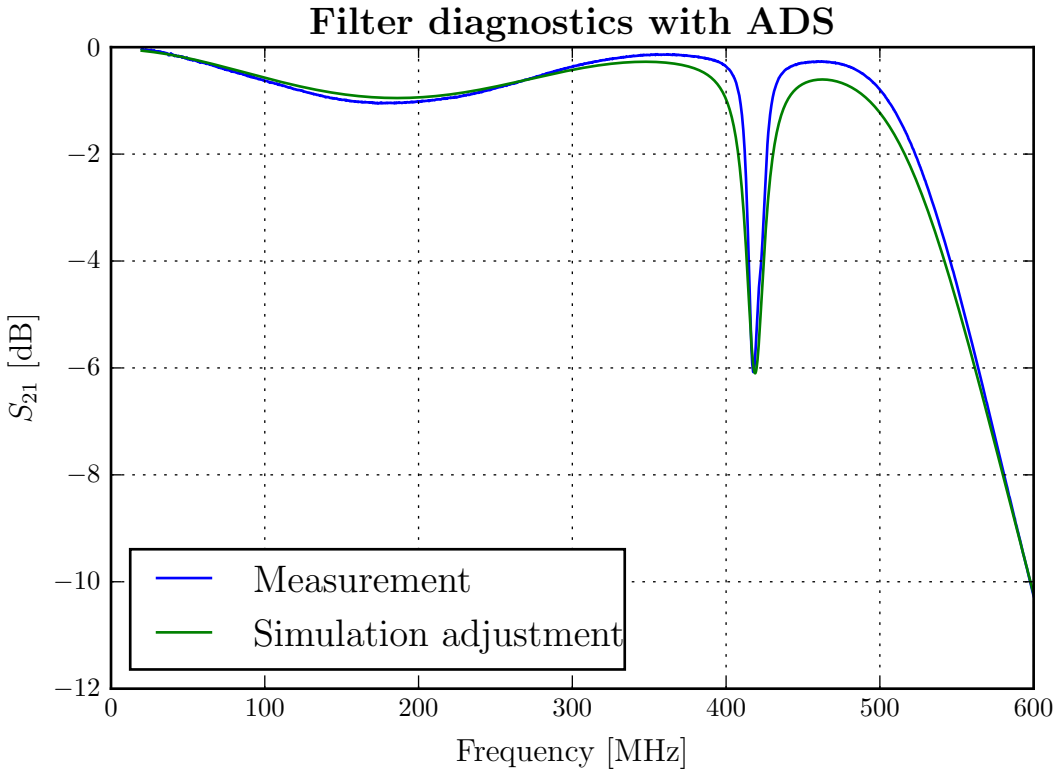

Figure 5.2: Filter diagnostic model matching

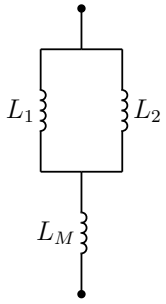

Figure 5.3: Equivalent circuit model for coupled parallel inductors

The following actions were taken to rectify the issues discussed: firstly, the resonator was revised to incorporate only a single inductor to eliminate the issue of coupling, secondly, the capacitive component of the resonator was reduced to only incorporate four varactor diodes and lastly, each resonator was biased separately to allow for greater control of the null placement. The final results of the filter are presented in figure 5.4.

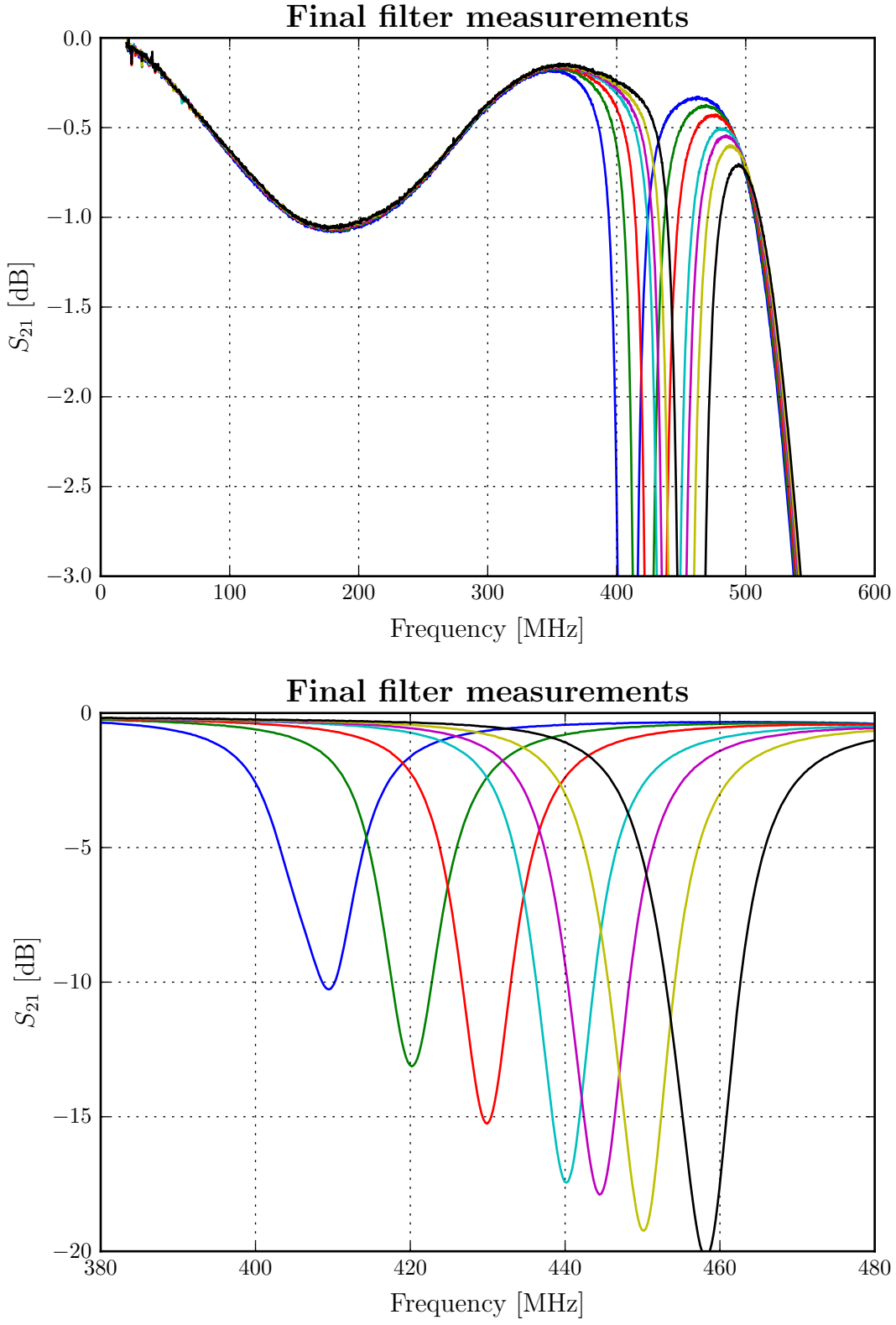

Figure 5.4: Final filter measurements

From the results in figure 5.4, it is clear that the performance of the filter is greatly improved and is more in line with what was initially predicted in ADS. The tuning range is 400-460MHz and the null rejection ranges between 10dB and 20dB.

5.2 Non-linear distortion measurements

The measurements of the non-linear behaviour of the filter were performed after the modifications had been made to it as explained in the previous section. A two-tone test was performed on the filter with the practical setup shown in figure 5.5. A wideband Mini-Circuits RF combiner with approximately 5.5dB insertion loss was used to combine the input signals from the signal generators. The output power of both signal generators was set to 0dBm and the frequencies of the fundamental tones were set as $f_1 = 445$MHz and $f_2 = 445.01$MHz. The notch of the filter was tuned down to around 400MHz with the diodes biased at approximately 12V. Figure 5.6 shows the results of the two-tone test obtained on the spectrum analyzer.

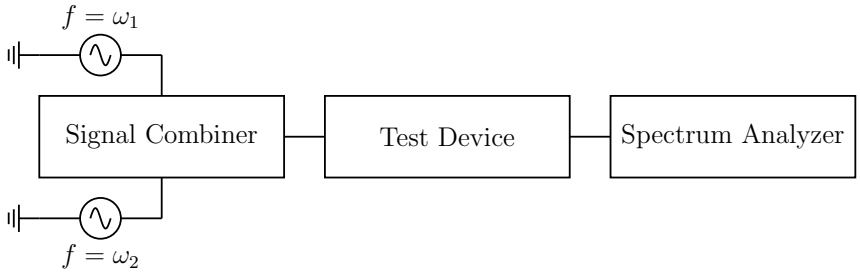

Figure 5.5: Diagram of practical setup for a two-tone test

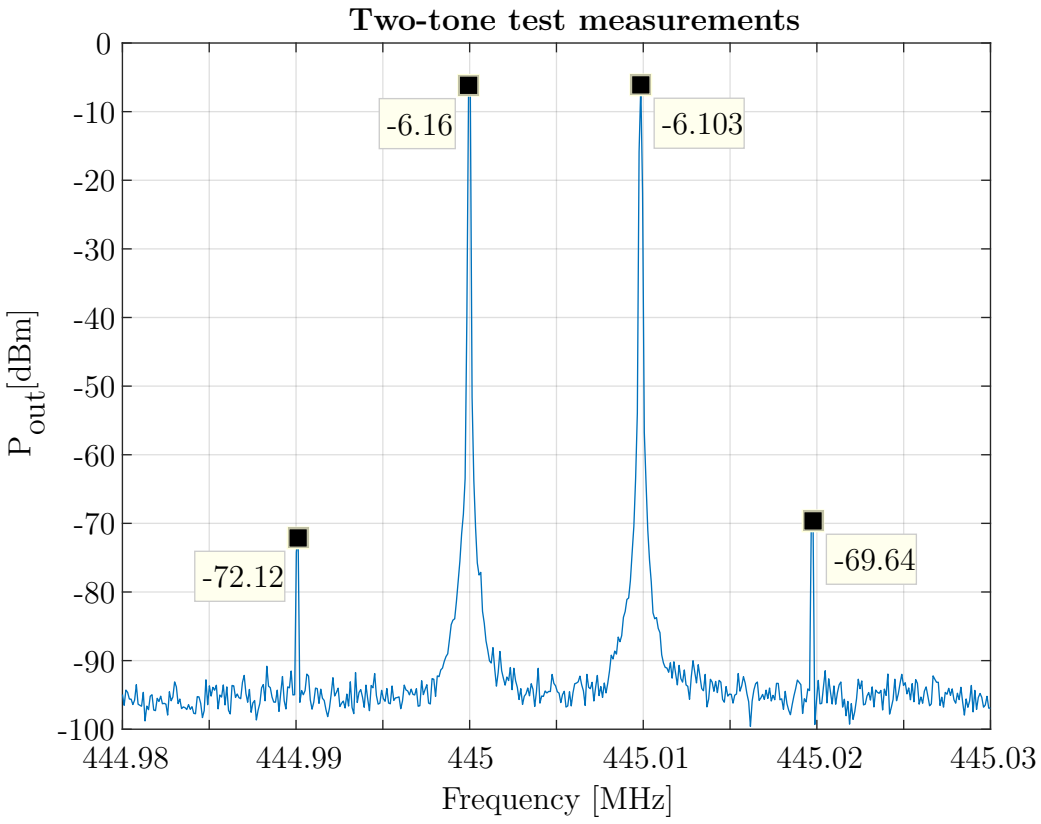

Figure 5.6: Two-tone test measurements

From the results in figure 5.6, ΔP is approximately 64dBm based on the largest IM product. The measured third-order intercept point is determined as 26dBm. The noise floor is approximately -90dBm and the SFDR is determined as 77dB. Although the SFDR is significantly lower than what was predicted in the simulation, it is still sufficient enough as it is greater than the dynamic range of the jammer receiver.

Chapter 6

Conclusion

The main objective of this thesis was to design a notch filter to suppress unwanted large signals in the UHF PMR band to improve the dynamic range of a receiver used by a jammer system. There was no rigid specification placed on the design as it was required to determine what performance could be achieved with current technology available.

In chapter 1, the project background was discussed in detail and the objectives of the thesis were stated. The characterisation of the performance of the jammer receiver gave insight into the need for a notch filter design to be pursued.

In chapter 2, filter theory was presented. A mathematical approach was initially pursued to investigate the different filter response types. A third-order Chebyshev (0.5dB ripple) filter response was found to be adequate to utilise. A circuit model was derived to implement the desired filter response.

In chapter 3, modelling techniques for different components were discussed in order to predict the behaviour of a given component at high frequencies. Components were chosen to realise the filter in circuitry and a simulation incorporating the modelling techniques was performed to predict the behaviour of the filter.

In chapter 4, basic theory was presented on how to characterise the dynamic range of the filter from a systems approach.

In chapter 5, results were presented for the measurements of both S-parameters and dynamic range capabilities of the filter. For a single filter, the tuning range is 400-460MHz with a null rejection varying between 10dB and 20dB. Two or three such filters could be connected in cascade to improve the overall null rejection. From these results it can be concluded that for new designs, caution should be taken if inductors are to be used in pairs as the coupling between them can decrease their overall Q-factors substantially. When

tuning resonators, it is best to implement separate control mechanisms to ensure that each resonator is fine tuned independently. A control system was designed with separate voltage output channels for such tuning purposes. A schematic of the control system is presented in appendix B.

Appendix A

Selected component datasheets

A.1 Coilcraft air core inductors

Web page | Sample & buy | Tools & software | Support & FAQ

Document 107-1

RoHS COMPLIANT

AEC Q200 -125°C

Mini Air Core Inductors

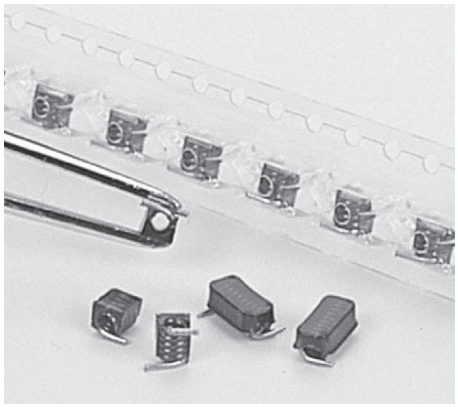

- Small air core inductors feature high Q and tight tolerances
- Acrylic jacket provides a flat top for pick and place
- Solder coated leads ensure reliable soldering

Terminations RoHS compliant tin-silver over copper. Other terminations available at additional cost.

Ambient temperature –40°C to +125°C with Irms current, +125°C to +140°C with derated current

Storage temperature Component: –40°C to +140°C. Tape and reel packaging: –40°C to +80°C

Resistance to soldering heat Max three 40 second reflows at +260°C, parts cooled to room temperature between cycles

Temperature Coefficient of Inductance (TCL) +5 to +70 ppm/°C

Moisture Sensitivity Level (MSL) 1 (unlimited floor life at <30°C / 85% relative humidity)

Failures in Time (FIT) / Mean Time Between Failures (MTBF) One per billion hours / one billion hours, calculated per Telcordia SR-332

Packaging A0xT: 700/7″ reel; 2500/13″ reel Plastic tape: 12 mm wide, 0.32 mm thick, 8 mm pocket spacing, 3.3 mm pocket depth
BxxT: 500/7″ reel; 2200/13″ reel Plastic tape: 16 mm wide, 0.28 mm thick, 8 mm pocket spacing, 3.4 mm pocket depth
Recommended pick and place nozzle: OD: 0.110″; ID: 0.091″

PCB washing Tested to MIL-STD-202 Method 215 plus an additional aqueous wash. See Doc787_PCB_Washing.pdf.

Part number[1]	Turns	L[2] (nH)	Percent tol[3]	Q[4] min	SRF min[5] (GHz)	DCR max[6] (mOhm)	Irms[7] (A)	Weight (mg)
A01TKL_	1	2.5	**10**	145	12.5	1.1	4	31
A02T_L_	2	5.0	**5,2**,1	140	6.5	1.8	4	42
A03T_L_	3	8.0	**5,2**,1	140	5.0	2.6	4	52
A04T_L_	4	12.5	**5,2**,1	137	3.3	3.4	4	65
A05T_L_	5	18.5	**5,2**,1	132	2.5	3.9	4	78
B06T_L_	6	17.5	**5,2**,1	100	2.2	4.5	4	100
B07T_L_	7	22.0	**5,2**,1	102	2.1	5.2	4	110
B08T_L_	8	28.0	**5,2**,1	105	1.8	6.0	4	118
B09T_L_	9	35.5	**5,2**,1	112	1.5	6.8	4	133
B10T_L_	10	43.0	**5,2**,1	106	1.2	7.9	4	147

1. When ordering, please specify **tolerance**, **termination** and **packaging** codes:
   A02TGLC
   Tolerance: **F** = 1% **G** = 2% **J** = 5% **K** = 10% (Table shows stock tolerances in bold.)
   Termination: **L** = RoHS compliant tin-silver (96.5/3.5) over copper. Special order: **T** = RoHS tin-silver-copper (95.5/4/0.5) or **S** = non-RoHS tin-lead (63/37).
   Packaging: **C** = 7″ machine-ready reel. EIA-481 embossed plastic tape, 700 (AxxT) or 500 (BxxT) parts per full reel.
   B = Less than full reel. In tape, but not machine-ready. To have a leader and trailer added ($25 charge), use code letter C instead.
   D = 13″ machine-ready reel. EIA-481 embossed plastic tape. Factory order only, not stocked, 2500 (AxxT) or 2200 (BxxT) parts per full reel.
2. Inductance measured at 150 MHz with an Agilent/HP 4286 or equivalent, a Coilcraft SMD-A and correlation.
3. Tolerances in bold are stocked for immediate shipment.
4. Q measured at 150 MHz using an Agilent/HP 4291A with an Agilent/HP 16193A test fixture or equivalents.
5. SRF tested on an Agilent/HP 8720D or equivalent and a Coilcraft SMD-D fixture.
6. DCR tested on the Cambridge Technology Model Micro-ohmmeter or equivalent.
7. Current that causes a 15°C temperature rise from 25°C ambient.
8. Electrical specifications at 25°C.

Refer to Doc 362 "Soldering Surface Mount Components" before soldering.

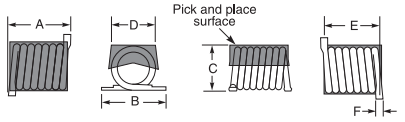

Size	A max	B max	C max	D	E	F max
A	0.155 3,94	0.175 4,45	0.124 3,15	0.110 ±0.010 2,79 ±0,25	0.115 ±0.010 2,92 ±0,25	0.029 0,74 inch mm
B	0.270 6,86				0.230 ±0.015 5,84 ±0,38	

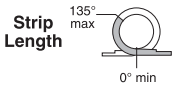

Recommended Land Patterns

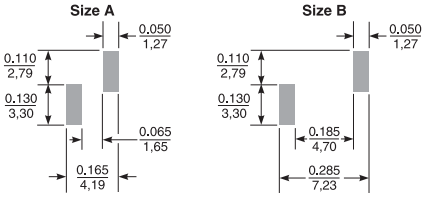

Dimensions are in inches / mm

Coilcraft
www.coilcraft.com

US +1-847-639-6400 sales@coilcraft.com
UK +44-1236-730595 sales@coilcraft-europe.com
Taiwan +886-2-2264 3646 sales@coilcraft.com.tw
China +86-21-6218 8074 sales@coilcraft.com.cn
Singapore + 65-6484 8412 sales@coilcraft.com.sg

Document 107-1 Revised 10/03/11

Document 107-2

Designer's Kit C302 contains 12 each of all 5% values
Designer's Kit C302-2 contains 12 each of all 2% values

Mini Air Core Inductors

Typical L vs Frequency

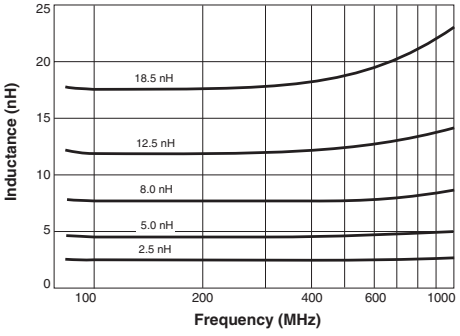

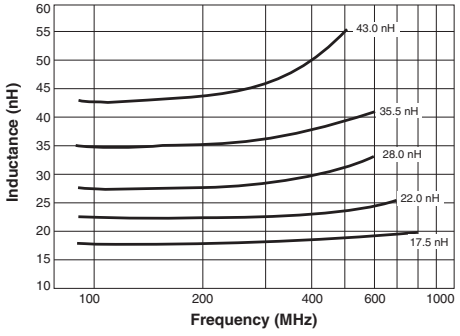

Typical Q vs Frequency

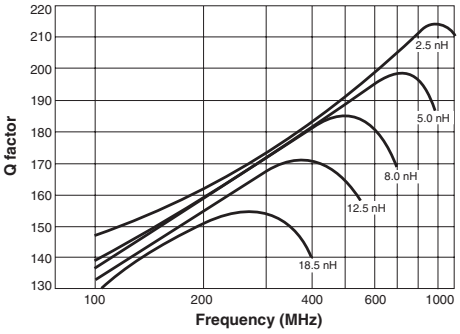

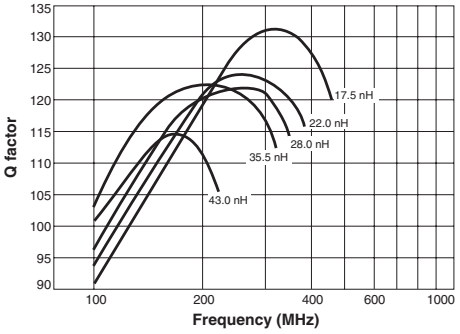

Typical Irms Derating

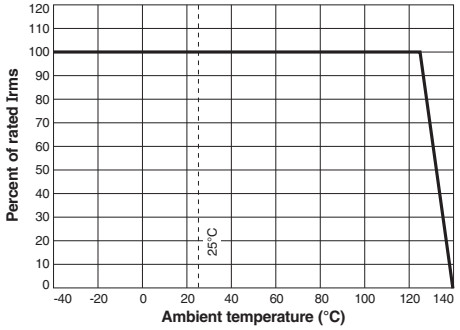

S-Parameter files
ON OUR WEB SITE

SPICE models
ON OUR WEB SITE

Coilcraft
www.coilcraft.com

US +1-847-639-6400 sales@coilcraft.com
UK +44-1236-730595 sales@coilcraft-europe.com
Taiwan +886-2-2264 3646 sales@coilcraft.com.tw
China +86-21-6218 8074 sales@coilcraft.com.cn
Singapore + 65-6484 8412 sales@coilcraft.com.sg

Document 107-2 Revised 10/03/11

A.2 Skyworks varactor diodes

SKYWORKS®

DATA SHEET

SMV1405 to SMV1430 Series: Plastic Packaged Abrupt Junction Tuning Varactors

Applications

- High-Q resonators in wireless system VCOs
- High volume commercial systems

Features

- High Q
- Low series resistance for low phase noise
- Packages rated MSL1, 260 °C per JEDEC J-STD-020

Skyworks Green™ products are compliant with all applicable legislation and are halogen-free. For additional information, refer to *Skyworks Definition of Green™*, document number SQ04-0074.

Description

The SMV1405 to SMV1430 group of silicon abrupt junction varactor diodes is designed for use in Voltage Controlled Oscillators (VCOs) requiring tight capacitance tolerances. The low resistance of these varactors makes them appropriate for high-Q resonators in wireless system VCOs to frequencies above 10 GHz. This family of varactors is characterized for capacitance over temperature.

Table 1 describes the various packages and markings of the SMV1405 to SMV1430 group of varactors.

Table 3. SMV1405 to SMV1430 Series Electrical Specifications[1]
(T_{OP} = 25 °C, Unless Otherwise Noted)

Part Number	C_T @ 0.5 V (pF)	C_T @ 1 V (pF)	C_T @ 4 V (pF)		$\frac{C_T \text{ @ 0 V}}{C_T \text{ @ 30 V}}$ (Ratio)	R_S @ 4 V, 500 MHz (Ω)	Q @ 4 V, 50 MHz
	Typ.	Typ.	Min.	Max.	Min	Max.	Typ.
SMV1405	2.1	1	1.21	1.45			3200
SMV1408	3.4	2	1.71	2.11			2900
SMV1413	7.4	6	3.64	4.42			2400
SMV1430	1.01				3.8	3.15	1680

[1] Performance is guaranteed only under the conditions listed in this table.

Reverse voltage V_R (I_R = 10 µA) = 30 V minimum
Reverse current I_R (V_R = 24 V) = 20 nA maximum

Total capacitance shown was measured in the SOT-23 single configuration with a typical case capacitance of 0.13 pF. The total capacitance may differ slightly for other packages/configurations.

Table 4. Capacitance vs Reverse Voltage[1]

V_R (V)	C_T (pF)			
	SMV1405	SMV1408	SMV1413	SMV1430
0	2.67	4.08	9.24	1.24
0.5	2.12	3.36	7.39	1.01
1.0	1.84	2.94	6.37	0.88
1.5	1.70	2.60	5.71	0.80
2.0	1.55	2.38	5.22	0.74
2.5	1.44	2.24	4.85	0.68
3.0	1.34	2.08	4.55	0.65
4.0	1.25	1.88	4.10	0.60
5.0	1.17	1.72	3.77	0.56
10.0	0.95	1.28	2.85	0.44
20.0	0.77	1.01	2.12	0.35
30.0	0.63	0.95	1.77	0.31

[1] Total capacitance shown was measured in the SOT-23 single configuration with a typical case capacitance of 0.13 pF. The total capacitance may differ slightly for other packages/configurations.

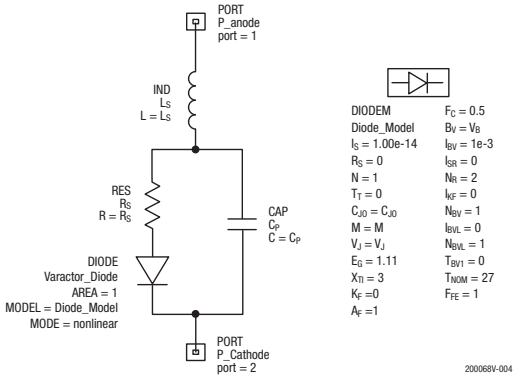

Figure 4. SPICE Model

Table 5. SPICE Model Parameters

Part Number	C_{J0} (pF)	V_J (V)	M	C_P (pF)	R_S (Ω)
SMV1405	2.37	0.77			0.80
SMV1408	3.89	0.92			0.60
SMV1413	8.92	0.87			0.35
SMV1430	1.11	0.86			3.15

Values extracted from measured performance.
For package inductance, L_S, refer to Table 1.
For more details, refer to the Skyworks Application Note, *Varactor SPICE Model for Approved RF VCO Applications*, document number 200315.

A.3 KEMET RF capacitors

Surface Mount Multilayer Ceramic Capacitors (SMD MLCCs) for High Power Applications

CBR Series, C0G Dielectric, Ultra High Q, Low ESR, 6.3VDC–250VDC (RF & Microwave)

The Capacitance Company KEMET CHARGED.

Overview

KEMET's CBR Series surface mount multilayer ceramic capacitors (MLCCs) in C0G dielectric feature a robust and exceptionally stable copper electrode dielectric system that offers excellent low loss performance (High Q). These devices provide extremely low ESR and high self-resonance characteristics, and are well-suited for resonant circuit applications or those where Q and stability of capacitance characteristics are required. CBR Series capacitors exhibit no change in capacitance with respect to time and voltage and boast a negligible change in capacitance with reference to ambient temperature. Capacitance change is limited to ±30 ppm/°C from -55°C to +125°C.

CBR Series devices are suitable for many circuit applications including RF power amplifiers, mixers, oscillators, low noise amplifiers, filter networks, antenna tuning, timing circuits, delay lines and MRI imaging coils.

HiQ-CBR RF & MICROWAVE

Benefits

- -55°C to +125°C operating temperature range
- Ultra high Q
- Base metal electrode (BME) dielectric system
- Pb-Free and RoHS Compliant
- 0201, 0402, 0603 and 0805 case sizes (inches)
- DC voltage ratings of 6.3 V, 10 V, 25 V, 50 V, 100 V and 250 V
- Capacitance offerings ranging from 0.1 pF up to 100 pF
- Available capacitance tolerances of ±0.05 pF, ±0.1 pF, ±0.25 pF, ±0.5 pF, ±1%, ±2%, ±5% and ±10%
- No piezoelectric noise
- Low ESR
- High thermal stability
- No capacitance change with respect to applied rated DC voltage
- Negligible capacitance change with respect to temperature
- No capacitance decay with time
- Non-polar device, minimizing installation concerns
- 100% pure matte tin-plated termination finish allowing for excellent solderability

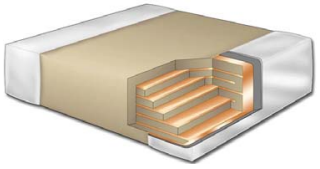

Ordering Information

CBR	02	C	330	F	9	G	A	C	
Series	Case Size (L"x W")	Specification/ Series	Capacitance Code (pF)	Capacitance Tolerance	Voltage	Dielectric	Termination Style	Termination Finish	Packaging/Grade (C-Spec)[1]
CBR	02 = 0201 04 = 0402 06 = 0603 08 = 0805	C = Standard	2 Sig. Digits + Number of Zeros Use 9 for 1.0 - 9.9 pF Use 8 for 0.5 - .99 pF ex. 2.2 pF = 229 ex. 0.5 pF = 508	A = ±0.05 pF B = ±0.1 pF C = ±0.25 pF D = ±0.5 pF F = ±1% G = ±2% J = ±5%	9 = 6.3V 8 = 10V 3 = 25V 5 = 50V 1 = 100V A = 250V	G = C0G	A = N/A	C = 100% Matte Sn	Blank = 7" Reel Unmarked

[1] *When ordering CBR series devices, a "suffix" or "Cspec" is not required to indicate a 7" reel packaging option. CBR devices are only available and shipped on 7" reels (paper tape). Bulk bag and cassette packaging options are not available. Please contact KEMET if you have a specific, non-standard packaging requirement.*

Electrical Characteristics cont'd

ESR vs. Frequency 0402

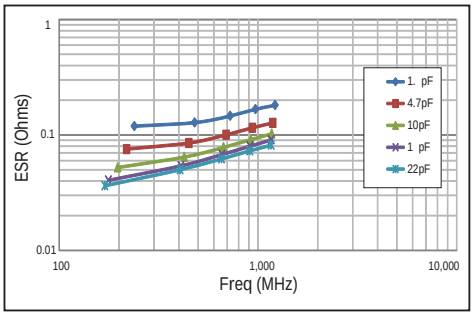

Q vs. Frequency 0402

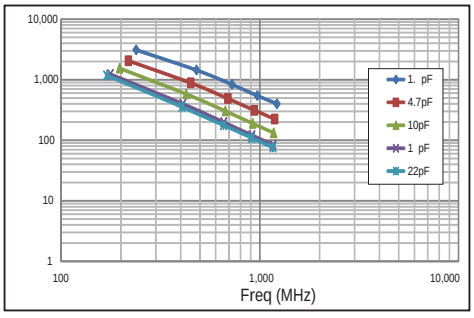

ESR vs. Frequency 0603

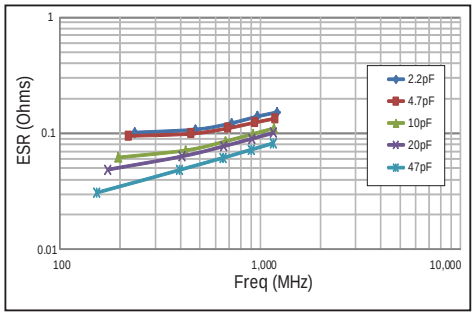

Q vs. Frequency 0603

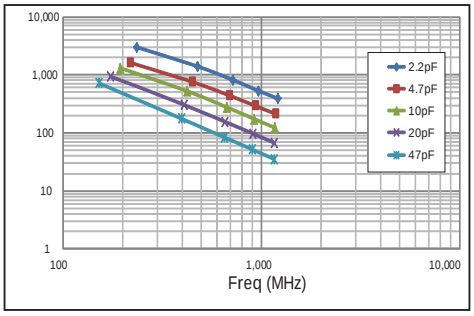

ESR vs. Frequency 0805

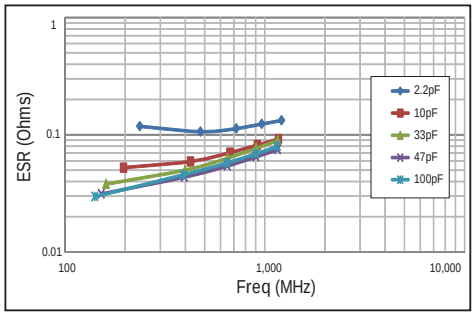

Q vs. Frequency 0805

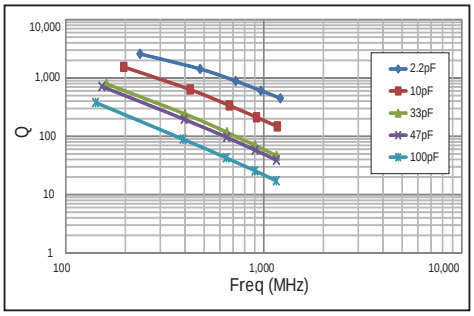

Appendix B

Control system schematic

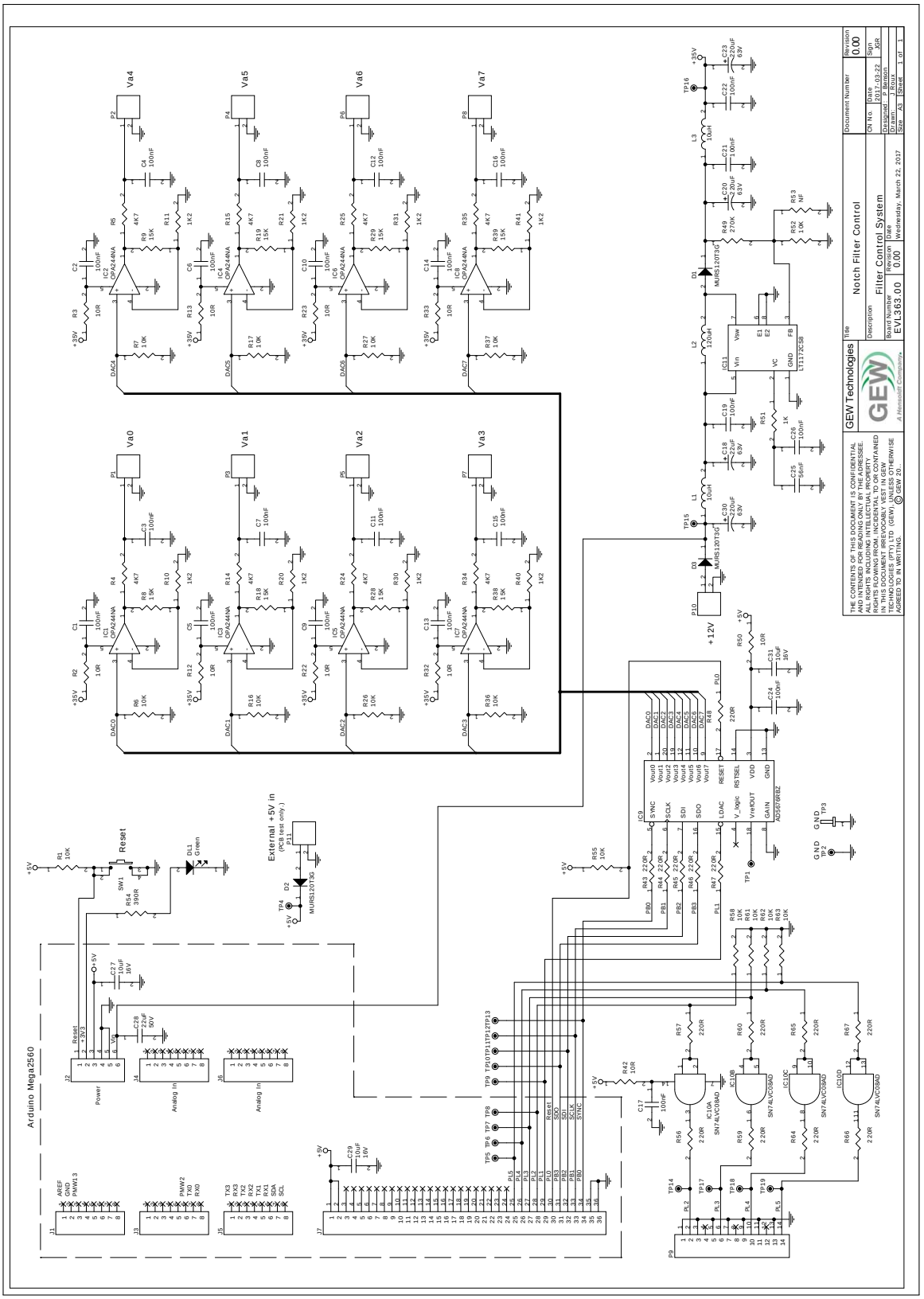

List of References

[1] D. L. Adamy, *Electronic warfare pocket guide*. SciTech Publishing, 2012.

[2] R. E. Mcshea, *Test and Evaluation of Aircraft Avionics and Weapon Systems*, 2nd ed. Institution of Engineering and Technology, 2014.

[3] R. A. Poisel, *Introduction to Communication Electronic Warfare Systems*, 2nd ed. Artech House, 2008.

[4] C. van Niekerk, "Jammer system notes," September 2016.

[5] S. J. Nightingale, "A workshop on rf interference suppression on fixed and mobile platforms," October 2013.

[6] P. Donaldson, "Jam sessions," *Digital Battlespace*, vol. 7, no. 6, pp. 12–17, Nov. 2015.

[7] J. Bonarius, "Adaptive noise and interference cancellation for mobile communications," Master's thesis, Stellenbosch University, 2016.

[8] D. M. Pozar, *Microwave and RF wireless systems*. J. Wiley & Sons, 2001.

[9] L. Besser and R. Gilmore, *Practical RF Circuit Design for Modern Wireless Systems*. Artech House, 2003, vol. I.

[10] D. M. Pozar, *Microwave Engineering*, 4th ed. J. Wiley & Sons, 2012.

[11] C. Coleman, *An Introduction to Radio Frequency Engineering*. Cambridge University Press, 2004.

[12] *VX-160EU/-180EU UHF FM Transceiver*, Vertex Standard, 2004.

[13] *VX-160EV/-180EV VHF FM Transceiver*, Vertex Standard, 2004.

[14] *Leopard I wideband military radio*, Satcom, 2012.

[15] Y.-C. Ou and G. M. Rebeiz, "Lumped-element fully tunable bandstop filters for cognitive radio applications," *IEEE Transactions on Microwave Theory and Techniques*, vol. 59, no. 10, pp. 2461–2468, 2011.

[16] M. B. Steer, *Microwave and RF Design: A Systems Approach.* SciTech Publishing, 2010.

[17] C. Bowick, *RF Circuit Design*, 2nd ed. Elsevier Science, 2011.

[18] K. W. Whites, "Electronic engineering 481 microwave engineering lecture notes," September 2013.

[19] A. I. Zverev, *Handbook of filter synthesis.* J. Wiley & Sons, 1967.

[20] R. Sorrentino and G. Bianchi, *Microwave and RF Engineering.* J. Wiley & Sons, 2010.

[21] C. J. Fourie, "Electronics 315 filter theory selected notes," June 2014.

[22] G. L. Matthaei, L. Young, and E. M. T. Jones, *Microwave Filters, Impedance-matching Networks, and Coupling Structures.* Artech House, 1985.

[23] P. Meyer, "Coupled resonator filters from low-pass ladder networks research notes," Jul. 2015.

[24] L. Green, "Rf-inductor modeling for the 21st century," *EDN*, vol. 46, no. 22, pp. 67–74, September 2001. [Online]. Available: http://search.proquest.com/docview/222430896/

[25] I. J. Bahl, *Lumped elements for RF and microwave circuits.* Artech House, 2003.

[26] J. J. Carr, *RF components and circuits*, 1st ed. Newnes, 2002.

[27] *Application note: Varactor diodes*, Skyworks Solutions, Inc., Aug. 2008.

[28] *Application note: DTC Theory of Operation*, Peregrine Semiconductor, 2011.

[29] *Park Advanced Circuitry Materials: Mercurywave 9350*, Park Electrochemical Corp.

[30] S. A. Maas, *Nonlinear microwave circuits.* Artech House, 1988.